P122 | Advanced Topics in Plasma Physics

Magnetic Reconnection

Instructor: Muni Zhou

Solar, magnetospheric, and laboratory examples introduce the problem of magnetic reconnection. The derivations develop magnetic diffusion and flux freezing, current-sheet formation, a reduced-MHD description of Alfvén waves and tearing instability, and the Sweet–Parker model. Plasmoid and collisionless reconnection then connect these foundations to particle acceleration, astrophysical applications, and the interaction between reconnection and turbulence.

Dartmouth College

Graduate plasma physics

Contents

1 Magnetic reconnection: phenomena and questions **1**
1.1 Solar flares: slow storage, explosive release . . . 1
1.2 From a connectivity change to a solar eruption . . . 2
1.3 Earth's magnetosphere: the Dungey cycle . . . 3
1.4 Tokamak sawteeth: buildup, crash, and recovery . . . 4
1.5 The questions these examples pose . . . 5

2 Induction, diffusion, and frozen magnetic flux **6**
2.1 The induction equation and its time scales . . . 6
2.2 Flux through a moving surface . . . 6

3 Formation of current sheets **7**
3.1 A stagnation flow and a magnetic-field reversal . . . 7
3.2 When does a non-ideal layer matter? . . . 8

4 Reduced MHD and tearing instability **9**
4.1 Ordering: which motions are retained? . . . 9
4.2 Stream function, flux function, vorticity, and current . . . 9
4.3 The equations and the meaning of every term . . . 10
4.4 Check: the same equations support Alfvén waves . . . 10
4.5 A reversing sheet: equilibrium and linearization . . . 11
4.6 The ideal outer region and the matching parameter . . . 12
4.7 The inner layer and the constant-flux approximation . . . 13
4.8 Large matching parameter and the fastest mode . . . 13
4.9 Onset in a forming sheet . . . 14

5 The Sweet–Parker model **15**
5.1 Geometry and assumptions . . . 15
5.2 Match the electric field outside and inside the sheet . . . 15
5.3 Incompressibility and the outflow speed . . . 15
5.4 Flux-transfer rate and reconnection time . . . 16
5.5 Is the Sweet–Parker rate fast enough? . . . 17

6 Sweet–Parker reconnection in simulations and experiments **17**

7 Is the Sweet–Parker current sheet stable? **18**
7.1 The plasmoid instability . . . 18
7.2 The nonlinear regime: hierarchical plasmoid chains . . . 19

8 Plasmoids in the laboratory, the Sun, and astrophysical systems **20**
8.1 Laboratory and solar examples . . . 20
8.2 Consequences of plasmoid formation . . . 20

9 Collisionless reconnection **23**

10 Challenges and astrophysical applications **23**
10.1 Why the problem remains difficult . . . 23
10.2 Particle acceleration, radiation, and black-hole environments . . . 23

11 The interaction between reconnection and turbulence **25**
11.1 Reconnection in a turbulent background . . . 25
11.2 Reconnection-mediated turbulence . . . 25

References **28**

Recommended Reading **32**

1 Magnetic reconnection: phenomena and questions

Magnetic reconnection changes which plasma regions are connected by magnetic field lines. A departure from ideal flux freezing in a small region allows a much larger magnetic structure to reorganize, converting stored magnetic energy into bulk motion, heat, and energetic particles. The opening figures show how this process appears in solar observations, Earth's magnetosphere, and a magnetically confined laboratory plasma.

1.1 Solar flares: slow storage, explosive release

Solar flares illustrate how reconnection can participate in an **explosive release of stored magnetic energy**. Photospheric motions and emerging magnetic flux gradually stress the coronal field, building magnetic free energy. During a flare, rapid reconnection allows the field to reorganize and releases that energy into plasma motion, heating, and accelerated particles; the resulting radiation makes the event visible [1]. The central question is: *how can a system loaded slowly release its energy so quickly?*

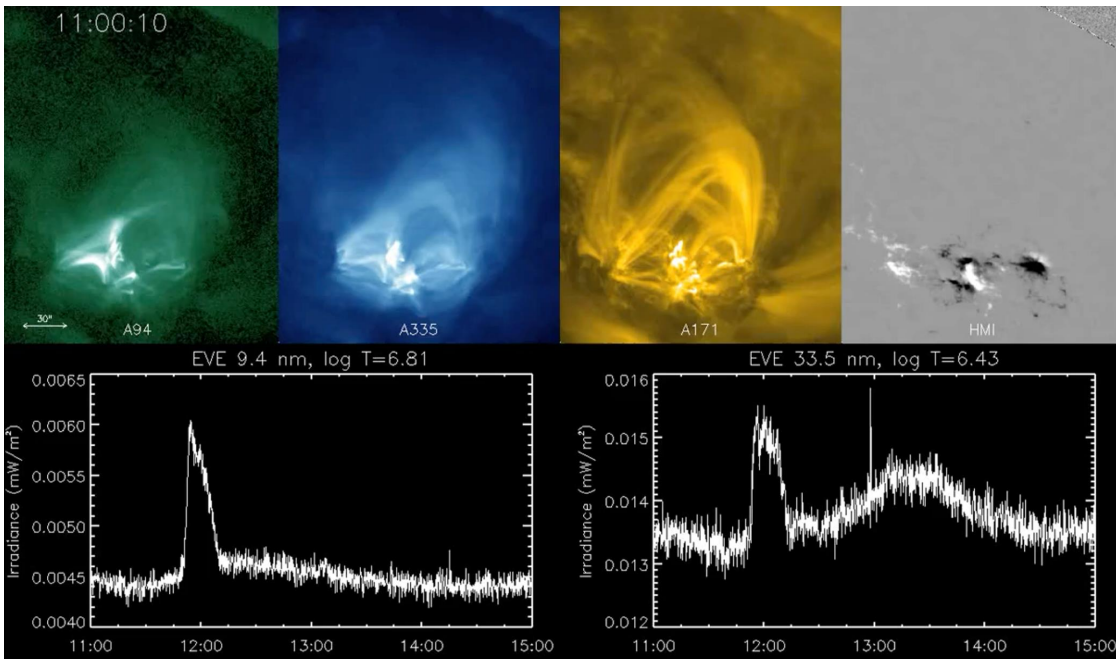


Figure 1: The 2010 May 5 flare: rapid EUV brightening followed by an extended radiative response. Image credit: NASA/SDO/EVE/AIA/HMI. The original NASA animation and panel guide identify and explain these observations [2].

Reading the panels. Across the top, A94, A335, and A171 are AIA extreme-ultraviolet images at 94, 335, and 171 Å: the hot component of 94 Å highlights flare-heated plasma, while 335 and 171 Å emphasize progressively cooler coronal plasma. The colours are assigned to the channels; brightness depends on emitting plasma and temperature response. The HMI magnetogram shows opposite line-of-sight photospheric magnetic polarities in black and white. Below, EVE measures full-disk irradiance at 9.4 and 33.5 nm (vertical axes) versus time in UT (horizontal axes). These are radiation measurements, rather than measurements of stored magnetic energy [2, 3].

The **explosive signature** is the abrupt rise near 12 UT, especially at 9.4 nm: the plasma brightens rapidly, then evolves more slowly. The broader, later 33.5 nm peak is the *EUV late phase*, emitted by a higher loop system [3]; it is not pre-flare buildup. These curves show the rapid radiative response, while the preceding magnetic-energy storage must be inferred from magnetic observations [1].

1.2 From a connectivity change to a solar eruption

The left panel of figure 2 isolates the local geometry. The red and blue curves approach a narrow layer with oppositely directed magnetic-field components. Small arrows on the curves indicate the field direction; the large yellow arrows show plasma flowing inward from above and below and outward to the left and right. The circled crosses mark a current into the page, associated with the field reversal.

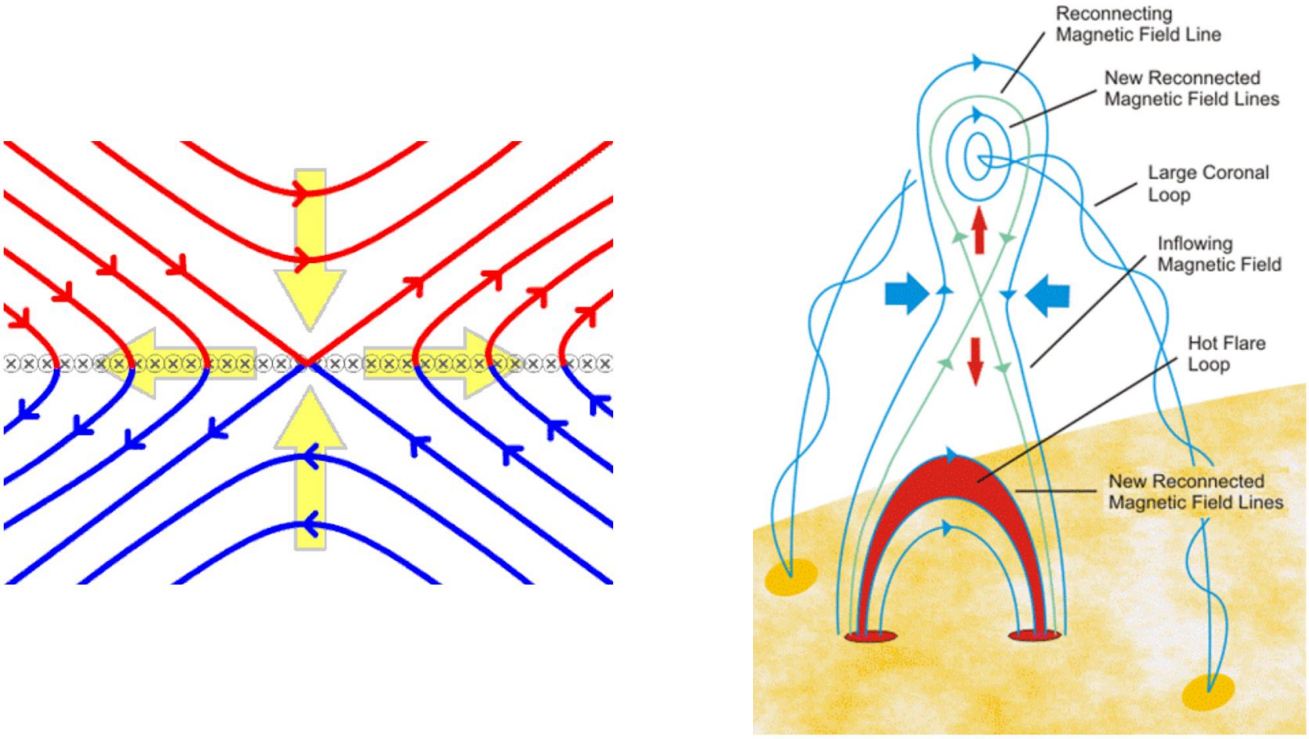


Figure 2: Left: inflow, a field reversal and current layer, and two reconnection outflows. Right: the same local process embedded in a solar magnetic structure, with an upward-moving structure and newly formed flare loops below. The right panel is a schematic, not an observational image. Solar schematic credit: NASA/SDO.

To identify reconnection, follow the connections: after passing through the non-ideal region, a line joins plasma regions that were previously on different lines. The newly connected field is sharply bent, and magnetic tension accelerates plasma away from the layer. The cartoon represents this connectivity change; it does not mean that magnetic field lines literally end or that $\nabla \cdot \boldsymbol{B}$ becomes nonzero.

The right panel places this geometry above the solar surface. Here the inflows are horizontal and the outflows vertical. Reconnection produces a lower set of loops connecting opposite photospheric polarities and an upper magnetic structure that can move outward. Energy transported into the lower loops and their footpoints contributes to the flare emission. This connects a localized change of connectivity to a large-scale eruption and heating. It also poses the scale-separation problem: how can a small non-ideal region process the flux and energy of a much larger system?

1.3 Earth's magnetosphere: the Dungey cycle

Figure 3 illustrates the **Dungey cycle**: circulation of magnetic flux and plasma through Earth's magnetosphere, driven here by solar wind carrying a southward interplanetary magnetic field (IMF). The wind flows from left to right. Red regions mark the two principal reconnection sites: the dayside magnetopause and the nightside magnetotail current sheet.

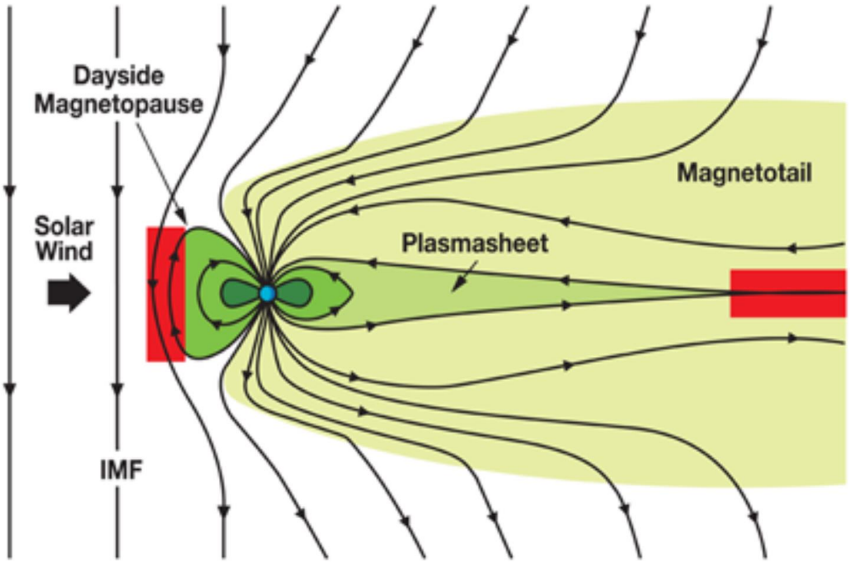


Figure 3: The Dungey cycle under southward IMF. Dayside reconnection opens terrestrial flux; nightside reconnection closes it again. Red regions mark reconnection sites schematically. Arrows along the curves indicate magnetic-field direction, not particle trajectories or convection velocities. The return of closed flux around Earth's flanks is not fully shown in this side view. Image credit: NASA.

Dayside reconnection opens magnetic flux. At the magnetopause, terrestrial field reconnects with the IMF. Closed field lines, with both ends connected to Earth, become open lines with one end connected to Earth and the other extending into the solar wind. This connection enables transfer of solar-wind energy, momentum, and plasma into the magnetosphere.

Convection transports open flux into the tail. The solar wind pulls the open flux tailward, stretching the field and storing magnetic energy in the tail lobes. The ionospheric footprints of the open field lines move across the polar caps from day to night. This stage mainly transports and deforms flux through approximately ideal motion.

Nightside reconnection closes flux and releases stored energy. Oppositely directed fields from the northern and southern tail lobes reconnect in the central current sheet. Reconnection produces newly closed terrestrial field lines on the earthward side and disconnected flux on the tailward side. Magnetic tension drives earthward and tailward outflows, converting magnetic energy into bulk motion, heating, and particle acceleration.

Closed flux returns to the dayside. Newly closed field lines contract earthward and then convect around the dawn and dusk flanks toward the dayside, completing the circulation. This three-dimensional return path corresponds to sunward flow at lower latitudes in the ionosphere, completing its two-cell convection pattern [43, 45].

The cycle follows magnetic flux, rather than a common orbit for all electrons and ions. Particles can also stream along field lines, remain trapped, or precipitate into the atmosphere. Auroral precipitation is distinct from the earthward bulk outflow.

1.4 Tokamak sawteeth: buildup, crash, and recovery

Figure 4 shows electron-temperature profiles reconstructed from electron cyclotron emission in a poloidal cross-section of the TFTR tokamak. The horizontal coordinates R and Z are spatial positions; height represents T_e in keV, and the colours show the temperature excess above a reference profile. The "mountain" is a temperature distribution, not the shape of the plasma [4].

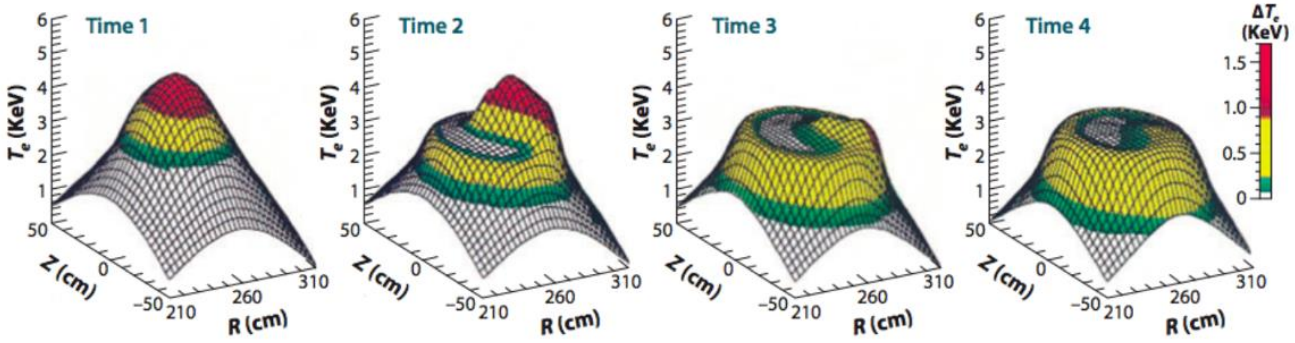


Figure 4: Four stages of a sawtooth crash, separated by approximately 120 μs. The hot core is initially peaked (Time 1), becomes displaced and distorted (Time 2), and rapidly flattens (Times 3–4). The slower buildup and subsequent recovery are not shown [4, 45].

During the slow buildup, continued heating raises the core temperature while the current and pressure profiles evolve. The magnetic field initially has nested flux surfaces that limit radial heat transport. In the standard sawtooth picture, a central region with safety factor $q < 1$ is surrounded by a $q = 1$ surface. Here q measures field-line winding: $q = 1$ means one toroidal turn per poloidal turn [45].

As the equilibrium evolves, a helical internal kink instability can grow, displacing the hot, current-carrying core. Its $m = n = 1$ structure has one variation around each of the poloidal and toroidal directions. The displacement concentrates current near the $q = 1$ surface and drives reconnection there: the instability supplies the deformation, and the non-ideal layer permits magnetic connections to change. The trigger depends on the current and pressure profiles and kinetic effects; $q < 1$ alone does not specify the crash time [45, 47].

The main temperature collapse in the figure occurs between Times 2 and 3. Rapid reconnection and heat redistribution belong to this crash stage, with the core largely flattened by Time 4. Newly connected field lines allow fast parallel electron heat transport between the hot core and cooler surrounding plasma, reducing the central temperature and warming the surrounding region. These temperature maps show when heat moves, but do not pinpoint the first instant of reconnection or imply complete reconnection: accompanying magnetic measurements in this experiment found only a partial relaxation of the field [4].

After the crash, the relaxed profiles reduce the instability drive. Continued heating and current-profile evolution rebuild the core until another crash occurs. The central temperature therefore shows a slow rise followed by a fast fall, repeatedly: this is the *sawtooth cycle* [47].

Ordinary sawteeth are common in tokamak fusion plasmas and are usually localized core relaxations, not catastrophic disruptions that terminate the discharge. Small, frequent sawteeth can even help prevent impurity accumulation in the core. Large crashes can, however, trigger other instabilities that degrade confinement, which is why sawtooth control matters [47].

1.5 The questions these examples pose

The examples lead to four connected questions:

1. **Rate: how fast does reconnection occur?** How rapidly does magnetic flux change its connections compared with an Alfvén crossing time?
2. **Onset: what triggers rapid reconnection?** Why can a stressed magnetic configuration persist and then begin reconnecting rapidly?
3. **Energy partition: where does the released energy go?** How much becomes bulk flow, ion heating, electron heating, or nonthermal particles?
4. **Modelling: how do we represent unresolved reconnection?** How can a simulation capture its effects when it cannot resolve the non-ideal layer?

We begin with induction and flux freezing to establish what ideal motion permits. Current-sheet formation then explains how small spatial scales arise; tearing describes an instability of those sheets; and the Sweet–Parker model provides a first estimate of a steady reconnection rate. The later applications return to the observational questions introduced here.

2 Induction, diffusion, and frozen magnetic flux

2.1 The induction equation and its time scales

The starting point is the resistive induction equation,

$$\frac{\partial \boldsymbol{B}}{\partial t} = \boldsymbol{\nabla} \times (\boldsymbol{u} \times \boldsymbol{B}) + \bar{\eta} \nabla^2 \boldsymbol{B}. \tag{2.1}$$

Given a plasma flow $\boldsymbol{u}$ and magnetic diffusivity $\bar{\eta}$, how does $\boldsymbol{B}$ evolve? We retain the distinction between electrical resistivity and magnetic diffusivity:

$$\boldsymbol{E} + \frac{\boldsymbol{u} \times \boldsymbol{B}}{c} = \eta \boldsymbol{j}, \qquad \boldsymbol{j} = \frac{c}{4\pi} \boldsymbol{\nabla} \times \boldsymbol{B}, \qquad \boxed{\bar{\eta} = \frac{\eta c^2}{4\pi}.} \tag{2.2}$$

Thus η is the coefficient in Ohm's law and $\bar{\eta}$ is the coefficient in the induction equation. The latter has dimensions of length squared divided by time. We take it to be spatially uniform in the estimates below.

If the field changes only by diffusion across a length L, then

$$\frac{B}{\tau_\eta} \sim \bar{\eta} \frac{B}{L^2}, \qquad \boxed{\tau_\eta \sim \frac{L^2}{\bar{\eta}}.} \tag{2.3}$$

Here τ_η is the characteristic time for resistivity to diffuse away a magnetic structure of amplitude B and length scale L, reducing its amplitude by an order-unity fraction.

For the solar corona, take $L \sim 10^4\,\mathrm{km}$ and a classical magnetic diffusivity $\bar{\eta} \sim 1\,\mathrm{m^2\,s^{-1}}$. Then τ_η is of order 10^6 years [46], whereas a typical flare lasts only 10 minutes to an hour. Diffusion alone is far too slow to explain a solar flare. We must therefore consider the nonlinear term $\boldsymbol{\nabla} \times (\boldsymbol{u} \times \boldsymbol{B})$, which couples plasma motion to magnetic-field evolution. Advection and stretching can form thin current sheets, where diffusion acts on a much shorter length scale.

For incompressible flow, $\boldsymbol{\nabla} \cdot \boldsymbol{u} = 0$, equation (2.1) becomes

$$\frac{\partial \boldsymbol{B}}{\partial t} + (\boldsymbol{u} \cdot \boldsymbol{\nabla})\boldsymbol{B} = (\boldsymbol{B} \cdot \boldsymbol{\nabla})\boldsymbol{u} + \bar{\eta} \nabla^2 \boldsymbol{B}, \qquad \boldsymbol{\nabla} \cdot \boldsymbol{B} = 0. \tag{2.4}$$

Comparing advection with diffusion on the same characteristic scale gives

$$\frac{|(\boldsymbol{u} \cdot \boldsymbol{\nabla})\boldsymbol{B}|}{|\bar{\eta} \nabla^2 \boldsymbol{B}|} \sim \frac{LU}{\bar{\eta}} \equiv \mathrm{Rm}. \tag{2.5}$$

If the relevant velocity is the Alfvén speed, the corresponding dimensionless number is

$$v_A = \frac{B}{\sqrt{4\pi\rho}}, \qquad \boxed{S = \frac{L v_A}{\bar{\eta}}}, \qquad \tau_{A,L} = \frac{L}{v_A}. \tag{2.6}$$

Both Rm and S can be very large. Representative estimates place solar-coronal S around 10^8–10^{14}, with values of order 10^8 also illustrating the magnetotail and tokamak cases. These are scale- and parameter-dependent estimates, using a macroscopic L.

2.2 Flux through a moving surface

Let a surface $S(t)$, bounded by $C(t)$, move with the plasma. Its magnetic flux is

$$\Psi = \int_{S(t)} \boldsymbol{B} \cdot \mathrm{d}\boldsymbol{S}. \tag{2.7}$$

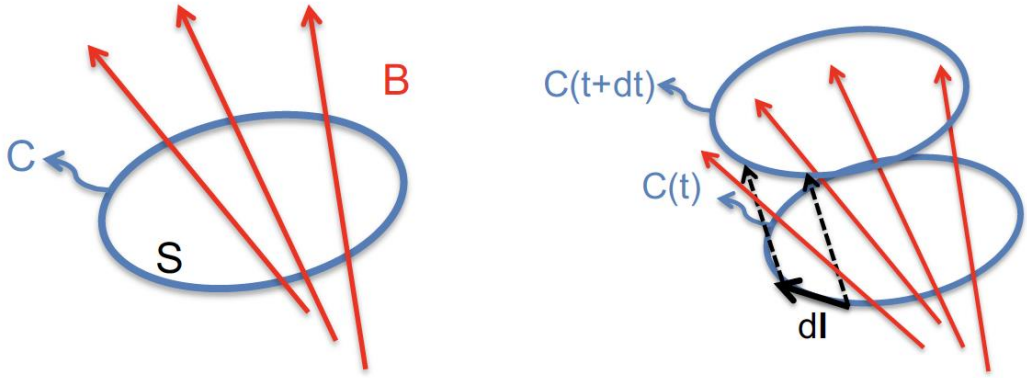


Figure 5: Magnetic flux through a surface bounded by a contour that moves with the plasma. The change includes both the local change in the field and the flux swept out by the moving boundary.

There are two contributions to its change: the field changes at a fixed point, and the surface moves. Keeping both,

$$\begin{aligned}\frac{\mathrm{d}\Psi}{\mathrm{d}t} &= \int_{S(t)} \frac{\partial \boldsymbol{B}}{\partial t}\cdot \mathrm{d}\boldsymbol{S} + \oint_{C(t)} \boldsymbol{B}\cdot(\boldsymbol{u}\times \mathrm{d}\boldsymbol{l}) \\ &= -c\int_{S(t)} (\boldsymbol{\nabla}\times\boldsymbol{E})\cdot \mathrm{d}\boldsymbol{S} - \int_{S(t)} \boldsymbol{\nabla}\times(\boldsymbol{u}\times\boldsymbol{B})\cdot \mathrm{d}\boldsymbol{S} \\ &= -c\int_{S(t)} \boldsymbol{\nabla}\times\left(\boldsymbol{E}+\frac{\boldsymbol{u}\times\boldsymbol{B}}{c}\right)\cdot \mathrm{d}\boldsymbol{S} \\ &= \boxed{-c\int_{S(t)} \boldsymbol{\nabla}\times(\eta\boldsymbol{j})\cdot \mathrm{d}\boldsymbol{S}.}\end{aligned} \tag{2.8}$$

For ideal Ohm's law, the right-hand side vanishes: magnetic flux is frozen into the flow. At finite resistivity, a sufficiently concentrated current can make the non-ideal term important locally even when macroscopic S is large. This motivates the next question: how does the plasma form a thin current sheet?

3 Formation of current sheets

3.1 A stagnation flow and a magnetic-field reversal

The Chapman–Kendall example uses a two-dimensional magnetic field and a flow that compresses in x while stretching in y. Writing an explicit constant field scale B_* in the field,

$$\boldsymbol{B} = B_*\left(\frac{y}{L(t)}, \frac{x}{a(t)}, 0\right), \qquad \boldsymbol{u} = (-\Gamma(t)x,\, \Gamma(t)y,\, 0). \tag{3.1}$$

The component B_y reverses across $x = 0$, and both fields are solenoidal. The simplest case takes $\Gamma(t) = \Gamma_0$, a constant.

Substitution into ideal induction gives the evolution of the two coefficients. For example,

$$\partial_t B_y + \boldsymbol{u}\cdot\boldsymbol{\nabla}B_y = -\frac{\dot{a}}{a}B_y - \Gamma_0 B_y, \qquad \boldsymbol{B}\cdot\boldsymbol{\nabla}u_y = \Gamma_0 B_y.$$

Therefore

$$\frac{\dot{a}}{a} = -2\Gamma_0, \qquad \frac{\dot{L}}{L} = 2\Gamma_0, \qquad \boxed{a(t) = a_0 e^{-2\Gamma_0 t}, \quad L(t) = L_0 e^{2\Gamma_0 t}.} \tag{3.2}$$

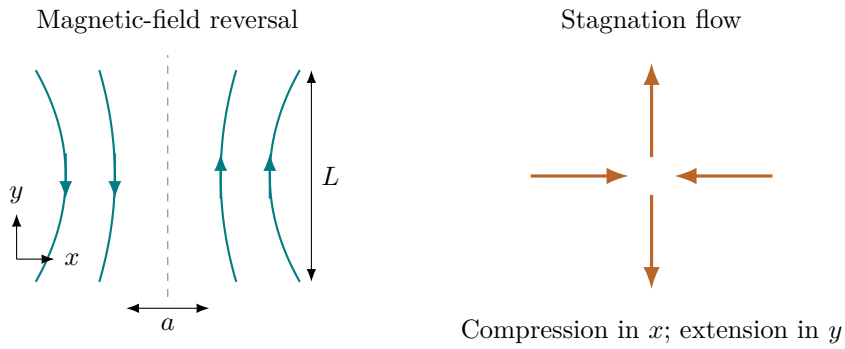


Figure 6: The field and flow geometry used to illustrate current-sheet formation. Here a and L parameterize the magnetic gradients in equation (3.1).

These factors of two follow from the field and flow in equation (3.1). The coefficient a sets the field gradient in this local linear-field model; it is not, by itself, the width of an entire advected magnetic profile.

The current is

$$j_z = \frac{cB_*}{4\pi}\left[\frac{1}{a(t)} - \frac{1}{L(t)}\right]. \tag{3.3}$$

Once $a \ll L$, the first term dominates and $j_z \propto e^{2\Gamma_0 t}$. Thus an initially smooth ideal flow can build a strong magnetic gradient.

3.2 When does a non-ideal layer matter?

Equation (2.8) shows why current concentration matters: resistivity is small, but $\eta \boldsymbol{j}$ need not remain negligible in a thin layer. The exact field in equation (3.1) is linear in position and has $\nabla^2 \boldsymbol{B} = 0$; it illustrates gradient growth. Resistive diffusion becomes important when the actual current-sheet profile develops the small-scale structure absent from that local ansatz.

Earth's magnetosphere provides two examples (figure 7). On the dayside, solar-wind pressure presses the solar-wind magnetic field against Earth's dipole field, forming a sharp field transition across the magnetopause current sheet. On the nightside, tailward stretching brings oppositely directed lobe fields together across the magnetotail current sheet [45]. Current concentration can develop through ideal deformation before non-ideal effects become important in the thin layers [5].

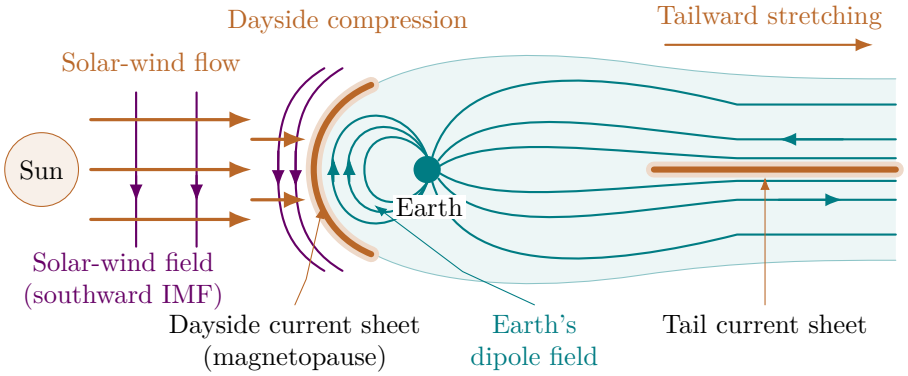


Figure 7: Solar-wind pressure compresses the purple solar-wind field against Earth's teal dipole field. Southward interplanetary magnetic field (IMF) is shown, opposite to the northward dayside field; near the boundary, the IMF is in the magnetosheath. Thick orange segments mark the dayside and tail current sheets. Orange arrows show flow or forcing; purple/teal arrows show field direction. Schematic, not to scale; the bow shock is omitted.

4 Reduced MHD and tearing instability

Tearing couples two processes: a magnetic perturbation drives a flow, and that flow changes the magnetic perturbation. Reduced MHD (RMHD) describes this coupling with a flux function and a stream function. We first specify the approximation and interpret its equations, check that they support Alfvén waves, and then use the same equations to calculate tearing growth.

4.1 Ordering: which motions are retained?

Take a straight, uniform guide field along $\hat{\boldsymbol{z}}$ and constant density ρ_0. **Throughout this section only, magnetic fields are expressed in velocity units:**

$$\boldsymbol{B} \equiv \frac{\boldsymbol{B}_{\text{physical}}}{\sqrt{4\pi\rho_0}}, \qquad \boldsymbol{B} = v_{A,g}\hat{\boldsymbol{z}} + \boldsymbol{B}_\perp, \qquad v_{A,g} = \frac{B_{g,\text{physical}}}{\sqrt{4\pi\rho_0}}. \tag{4.1}$$

We write the velocity as $\boldsymbol{U}$. The subscript $\perp$ refers to the (x, y) plane, perpendicular to the guide field. A standard Alfvénic RMHD ordering is

$$\boxed{\frac{B_\perp}{v_{A,g}} \sim \frac{U_\perp}{v_{A,g}} \sim \frac{k_\parallel}{k_\perp} \sim \epsilon \ll 1, \qquad \frac{|\omega|}{k_\perp v_{A,g}} \sim \epsilon.} \tag{4.2}$$

Here $k_\parallel$ measures variation along the *guide field*, $k_\perp$ measures variation across it, and ω is a characteristic fluctuation frequency. The ordering means small field-line tilts, transverse speeds small compared with the guide-field Alfvén speed, structures elongated along the guide field, and dynamics slow compared with a perpendicular Alfvén crossing. Small amplitudes do not remove the nonlinear terms: $U_\perp k_\perp$ can be comparable to $v_{A,g}k_\parallel$ because the perpendicular gradients are larger.

This ordering constructs the model; particular solutions can have still slower evolution or vanishing $k_\parallel$. It does not require the velocity and magnetic perturbations of a growing tearing mode to have equal amplitudes. We retain the transverse, incompressible Alfvénic dynamics. Density fluctuations, parallel flows, and compressive magnetosonic waves are not evolved in the two-field model used here. For classical resistive tearing we take uniform magnetic diffusivity $\bar{\eta}$ and neglect viscosity. As before, $\bar{\eta}$ is magnetic diffusivity, not the electrical resistivity η in Ohm's law.

4.2 Stream function, flux function, vorticity, and current

Define the stream function ϕ and flux function ψ by

$$\boxed{\boldsymbol{U}_\perp = \hat{\boldsymbol{z}} \times \boldsymbol{\nabla}_\perp \phi, \qquad \boldsymbol{B}_\perp = \hat{\boldsymbol{z}} \times \boldsymbol{\nabla}_\perp \psi.} \tag{4.3}$$

In components, $(U_x, U_y) = (-\partial_y\phi, \partial_x\phi)$ and $(B_x, B_y) = (-\partial_y\psi, \partial_x\psi)$. Both fields are automatically divergence-free in the perpendicular plane. The contours of ϕ are instantaneous streamlines. The contours of ψ trace the transverse magnetic field at fixed z; when $\partial_z = 0$, a full magnetic field line stays on a surface of constant ψ. Differences in ψ give transverse magnetic flux per unit length in z, in the velocity-unit normalization. Both ϕ and ψ have dimensions of length squared divided by time.

Taking one curl gives

$$\boxed{(\boldsymbol{\nabla} \times \boldsymbol{U})_z = \nabla_\perp^2 \phi, \qquad (\boldsymbol{\nabla} \times \boldsymbol{B})_z = \nabla_\perp^2 \psi.} \tag{4.4}$$

Thus $\nabla_\perp^2\phi$ is the guide-direction vorticity: it measures local rotation of the transverse flow. The quantity $\nabla_\perp^2\psi$ measures the guide-direction current, with the conversion to physical current density

$$j_{z,\text{physical}} = \frac{c\sqrt{4\pi\rho_0}}{4\pi}\nabla_\perp^2\psi. \tag{4.5}$$

A sharply curved flux function therefore means a strong current. The flux function itself is not the current, just as the stream function itself is not the vorticity.

4.3 The equations and the meaning of every term

Use the Poisson bracket convention

$$[f, g] \equiv \hat{\boldsymbol{z}} \cdot (\boldsymbol{\nabla}_\perp f \times \boldsymbol{\nabla}_\perp g) = \partial_x f \, \partial_y g - \partial_y f \, \partial_x g. \tag{4.6}$$

The definitions immediately give two useful identities for any scalar f:

$$[\phi, f] = \boldsymbol{U}_\perp \cdot \boldsymbol{\nabla}_\perp f, \qquad [\psi, f] = \boldsymbol{B}_\perp \cdot \boldsymbol{\nabla}_\perp f. \tag{4.7}$$

A bracket is therefore a directional derivative. Its physical role depends on whether the direction is set by the flow or by the magnetic field.

The resistive RMHD equations are

$$\boxed{\partial_t \psi + [\phi, \psi] = v_{A,g} \partial_z \phi + \bar{\eta} \nabla_\perp^2 \psi,} \tag{4.8}$$

$$\boxed{\partial_t \nabla_\perp^2 \phi + [\phi, \nabla_\perp^2 \phi] = v_{A,g} \partial_z \nabla_\perp^2 \psi + [\psi, \nabla_\perp^2 \psi].} \tag{4.9}$$

The first is the induction equation expressed in terms of magnetic flux. The second is the guide-direction curl of the momentum equation: taking a curl eliminates the pressure gradient. We use these equations without carrying out the full asymptotic reduction of MHD.

Flux equation. The term $\partial_t \psi$ is the change of flux function at a fixed location. The bracket $[\phi, \psi] = \boldsymbol{U}_\perp \cdot \boldsymbol{\nabla}_\perp \psi$ describes its advection by the transverse flow. In a two-dimensional ideal system their sum vanishes: the flux function is carried with the plasma. The term $v_{A,g} \partial_z \phi$ describes bending the guide field when neighbouring positions along it move differently. The term $\bar{\eta} \nabla_\perp^2 \psi$ is resistive diffusion; it permits magnetic flux to slip relative to the flow and allows magnetic connectivity to change.

Vorticity equation. The term $\partial_t \nabla_\perp^2 \phi$ is the local change of vorticity. The bracket $[\phi, \nabla_\perp^2 \phi]$ is advection of vorticity by the fluid. The term $v_{A,g} \partial_z \nabla_\perp^2 \psi$ is the linear magnetic-tension contribution to the vorticity evolution. The bracket $[\psi, \nabla_\perp^2 \psi]$ is the nonlinear magnetic-tension contribution: it measures variation of the current-related quantity along the transverse magnetic field and can drive or modify the flow's vorticity. It is not advection of vorticity by the fluid.

The two magnetic terms can be read together as

$$v_{A,g} \partial_z \nabla_\perp^2 \psi + [\psi, \nabla_\perp^2 \psi] = (\boldsymbol{B} \cdot \boldsymbol{\nabla}) \nabla_\perp^2 \psi. \tag{4.10}$$

This is the guide-direction curl of magnetic tension in the retained dynamics. Magnetic pressure is part of the pressure gradient removed by the curl. Thus the two equations describe a feedback: the flow bends or advects magnetic flux, and magnetic tension changes the flow.

4.4 Check: the same equations support Alfvén waves

Linearize about the uniform guide field with no transverse equilibrium field or flow. Products of perturbations, including the Poisson brackets, vanish at linear order. Set $\bar{\eta} = 0$ to isolate wave propagation:

$$\partial_t \psi = v_{A,g} \partial_z \phi, \qquad \partial_t \nabla_\perp^2 \phi = v_{A,g} \partial_z \nabla_\perp^2 \psi. \tag{4.11}$$

For a Fourier mode with $k_\perp \neq 0$, the factor $-k_\perp^2$ cancels from the second equation, giving $\partial_t \phi = v_{A,g} \partial_z \psi$. Taking another time derivative yields

$$\partial_t^2 \psi = v_{A,g}^2 \partial_z^2 \psi. \tag{4.12}$$

For propagating modes proportional to $\exp[i(\boldsymbol{k}_\perp \cdot \boldsymbol{x}_\perp + k_\parallel z - \omega t)]$, with $k_\parallel \neq 0$,

$$\boxed{\omega^2 = k_\parallel^2 v_{A,g}^2, \qquad \phi = -\frac{\omega}{k_\parallel v_{A,g}} \psi.} \tag{4.13}$$

For the propagating modes, $\phi = \mp\psi$ on the $\omega = \pm k_\parallel v_{A,g}$ branches, so $\boldsymbol{U}_\perp = \mp\boldsymbol{B}_\perp$. A transverse motion bends field lines; magnetic tension provides the restoring response, producing a shear-Alfvén wave travelling in either direction along the guide field.

For tearing we now add a reversing transverse equilibrium field and choose perturbations independent of z. The explicit guide-field derivatives vanish, but the magnetic brackets remain. Setting $\partial_z = 0$ does *not* remove magnetic tension: the reversing field still couples flux and flow through those brackets.

4.5 A reversing sheet: equilibrium and linearization

Take the equilibrium, in the velocity units of equation (4.1), to be

$$\boldsymbol{B}_0 = v_{A,g}\hat{\boldsymbol{z}} + B_y(x)\hat{\boldsymbol{y}}, \qquad B_y(x) = v_A \tanh(x/a), \qquad \boldsymbol{U}_0 = 0. \tag{4.14}$$

Here v_A is the Alfvén speed based on the *reconnecting* field far from the reversal, whereas $v_{A,g}$ is based on the guide field. The strong-guide-field realization has $v_A \ll v_{A,g}$. The pressure balances the transverse magnetic pressure. Treat the sheet as quasi-static on the instability time: its slow resistive diffusion can be neglected while the perturbation grows.

The equilibrium flux function obeys $\psi_0' = B_y$, so one choice is $\psi_0 = a v_A \ln\cosh(x/a)$. Let

$$\psi = \psi_0(x) + \psi_1(x)e^{iky+\gamma t}, \qquad \phi = \phi_1(x)e^{iky+\gamma t}, \qquad \partial_z = 0. \tag{4.15}$$

The amplitudes ψ_1 and ϕ_1 describe the magnetic and velocity perturbations; primes below mean $\mathrm{d}/\mathrm{d}x$. In particular $B_{1x} = -ik\psi_1$ and $U_{1x} = -ik\phi_1$. We seek the linear growth rate $\gamma(k)$, not a steady reconnection rate or the final magnetic-island size. Keep three lengths distinct: the equilibrium sheet thickness a, the along-sheet scale k^{-1}, and the much smaller non-ideal layer width δ_{in}.

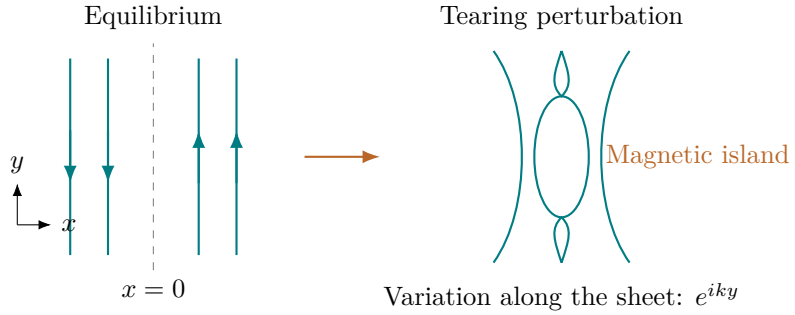


Figure 8: A reversing field and the island structure associated with tearing. The equilibrium varies across the sheet; the perturbation varies along it.

Only the equilibrium–perturbation brackets survive linearization. In the induction equation,

$$[\phi_1 e^{iky}, \psi_0] = -ikB_y\phi_1 e^{iky}. \tag{4.16}$$

In the vorticity equation, the flow-advection bracket is quadratic and drops out, while the magnetic bracket gives two terms:

$$[\psi_0, \nabla_\perp^2(\psi_1 e^{iky})] = ikB_y(\psi_1'' - k^2\psi_1)e^{iky}, \tag{4.17}$$

$$[\psi_1 e^{iky}, \psi_0''] = -ikB_y''\psi_1 e^{iky}. \tag{4.18}$$

Suppressing the common exponential therefore gives

$$\boxed{\gamma\psi_1 = ikB_y\phi_1 + \bar{\eta}(\psi_1'' - k^2\psi_1),} \tag{4.19}$$

$$\boxed{\gamma(\phi_1'' - k^2\phi_1) = ik\left[B_y(\psi_1'' - k^2\psi_1) - B_y''\psi_1\right].} \tag{4.20}$$

The first equation describes flux growth, motion across the equilibrium flux gradient, and resistive diffusion. The second balances the change of flow vorticity against magnetic driving: the equilibrium field acts on the perturbed current, and the perturbed field samples the equilibrium current gradient. These are the two magnetic brackets just evaluated.

At the neutral line, $B_y(0) = 0$, so

$$\gamma\psi_1(0) = \bar{\eta}[\psi_1''(0) - k^2\psi_1(0)]. \tag{4.21}$$

A regular growing reconnecting perturbation with $\psi_1(0) \neq 0$ therefore needs a non-ideal term. Its free energy comes from the equilibrium magnetic field; resistivity enables the connectivity change.

4.6 The ideal outer region and the matching parameter

Define the sheet-scale times and Lundquist number using the reconnecting field:

$$\tau_{A,a} = \frac{a}{v_A}, \qquad \tau_{\eta,a} = \frac{a^2}{\bar{\eta}}, \qquad S_a = \frac{av_A}{\bar{\eta}} \gg 1. \tag{4.22}$$

The classical tearing calculation assumes $\tau_{\eta,a}^{-1} \ll \gamma \ll kv_A$. The background diffuses slowly, while the outer magnetic field adjusts rapidly compared with the growth. Away from $x = 0$, neglect resistivity and then the small inertial term in equation (4.20). This gives

$$\boxed{\psi_1'' - \left(k^2 + \frac{B_y''}{B_y}\right)\psi_1 = 0,} \qquad \phi_1 = \frac{\gamma\psi_1}{ikB_y}. \tag{4.23}$$

Solve separately on either side, with perturbations decaying far from the sheet. The outer solution fixes the slope change that the inner solution must accommodate:

$$\boxed{\Delta' \equiv \frac{\psi_{1,\mathrm{out}}'(0^+) - \psi_{1,\mathrm{out}}'(0^-)}{\psi_{1,\mathrm{out}}(0)}.} \tag{4.24}$$

Here $0^\pm$ denote extrapolation of the outer solutions towards the centre. The apparent derivative jump is smoothed within the resistive layer; it is not a discontinuity of the actual finite-resistivity solution. In this classical model, $\Delta' > 0$ gives the unstable tearing branch.

For the Harris profile, a decaying solution on $x > 0$ is

$$\psi_{1,\mathrm{out}} = Ce^{-kx}\left[1 + \frac{\tanh(x/a)}{ka}\right], \qquad k > 0. \tag{4.25}$$

Use its even continuation on $x < 0$. Evaluating the value and slope at the centre,

$$\psi_{1,\mathrm{out}}(0) = C, \qquad \psi_{1,\mathrm{out}}'(0^+) = C\left(-k + \frac{1}{ka^2}\right), \qquad \psi_{1,\mathrm{out}}'(0^-) = -\psi_{1,\mathrm{out}}'(0^+),$$

so

$$\boxed{\Delta' a = 2\left(\frac{1}{ka} - ka\right).} \tag{4.26}$$

Thus $ka < 1$ is unstable, and $\Delta' a \sim (ka)^{-1}$ at long wavelengths. The outer problem supplies the magnetic geometry and matching condition. It does not yet determine how quickly the central layer can reconnect.

4.7 The inner layer and the constant-flux approximation

Inside $\delta_{\rm in} \ll a$, approximate $B_y \simeq v_A x/a$. Since $k\delta_{\rm in} \ll 1$, transverse derivatives dominate over k. The leading inner equations are

$$\gamma\psi_1 \simeq ik\frac{v_A x}{a}\phi_1 + \bar{\eta}\psi_1'', \qquad \gamma\phi_1'' \simeq ik\frac{v_A x}{a}\psi_1''. \tag{4.27}$$

In the FKR or constant-ψ regime, the perturbation flux is nearly uniform *across the layer*, with typical value ψ_c. It still grows in time. Matching to the outer solution requires the derivative to change by approximately $\Delta'\psi_c$ over a distance $\delta_{\rm in}$, giving

$$\psi_1'' \sim \frac{\Delta'\psi_c}{\delta_{\rm in}}, \qquad \frac{\text{change of } \psi_1 \text{ across the layer}}{\psi_c} \sim \Delta'\delta_{\rm in} \ll 1. \tag{4.28}$$

A small fractional change of flux does not mean a small curvature or current: the change occurs over a very short distance. Using $\psi_1'' \sim \psi_c/\delta_{\rm in}^2$ here would incorrectly assume an order-unity change across the layer.

Ignoring phase factors and order-unity coefficients, three amplitude balances suffice:

$$\gamma\psi_c \sim \bar{\eta}\frac{\Delta'\psi_c}{\delta_{\rm in}}, \qquad \text{growth and diffusion at the centre,} \tag{4.29}$$

$$\gamma\psi_c \sim k\frac{v_A\delta_{\rm in}}{a}\phi_{\rm in}, \qquad \text{flux growth and plasma motion,} \tag{4.30}$$

$$\gamma\frac{\phi_{\rm in}}{\delta_{\rm in}^2} \sim k\frac{v_A\delta_{\rm in}}{a}\frac{\Delta'\psi_c}{\delta_{\rm in}}, \qquad \text{flow inertia and magnetic driving.} \tag{4.31}$$

Here $\phi_{\rm in}$ is the typical stream-function amplitude at $|x| \sim \delta_{\rm in}$. These are compatible balances across the layer, rather than an assertion that every term is equal at every point.

The first relation gives $\gamma \sim \bar{\eta}\Delta'/\delta_{\rm in}$. Eliminating $\phi_{\rm in}$ between the other two gives

$$\gamma^2 \sim \left(\frac{kv_A}{a}\right)^2 \Delta'\delta_{\rm in}^3.$$

Substituting $\delta_{\rm in} \sim \bar{\eta}\Delta'/\gamma$ then yields

$$\gamma^5 \sim \left(\frac{kv_A}{a}\right)^2 \bar{\eta}^3(\Delta')^4.$$

In sheet-scale units the FKR results are [7]

$$\boxed{\gamma\tau_{A,a} \sim S_a^{-3/5}(ka)^{2/5}(\Delta' a)^{4/5}, \qquad \frac{\delta_{\rm in}}{a} \sim S_a^{-2/5}(ka)^{-2/5}(\Delta' a)^{1/5}.} \tag{4.32}$$

The growth rate combines the outer matching condition, magnetic driving, and inner diffusion. At fixed equilibrium and wavenumber, lowering resistivity slows this classical instability. Check $\Delta'\delta_{\rm in} \ll 1$ before applying the result.

4.8 Large matching parameter and the fastest mode

For the Harris sheet at $ka \ll 1$, the FKR growth rate becomes $\gamma\tau_{A,a} \sim S_a^{-3/5}(ka)^{-2/5}$: longer wavelengths grow faster along this branch. But Δ' increases as k decreases, eventually violating $\Delta'\delta_{\rm in} \ll 1$.

When the flux changes by order unity across the inner layer, use $\psi_1'' \sim \psi_1/\delta_{\rm in}^2$ instead. The same inner equations now give

$$\gamma \sim \frac{\bar\eta}{\delta_{\rm in}^2}, \qquad \gamma \sim k v_A \frac{\delta_{\rm in}}{a}. \tag{4.33}$$

Combining them gives the large-Δ' or Coppi scalings [6]:

$$\boxed{\gamma\tau_{A,a} \sim S_a^{-1/3}(ka)^{2/3}, \qquad \frac{\delta_{\rm in}}{a} \sim S_a^{-1/3}(ka)^{-1/3}.} \tag{4.34}$$

This branch grows faster towards larger k, unlike the long-wavelength FKR branch. The fastest mode lies near their transition, where $\Delta'\delta_{\rm in} \sim 1$. Using the Harris relation $\Delta' a \sim (ka)^{-1}$ gives $\delta_{\rm in}/a \sim ka$. Substitute the Coppi width to obtain

$$\boxed{k_{\max} a \sim S_a^{-1/4}, \qquad \delta_{\rm in,max}/a \sim S_a^{-1/4}.} \tag{4.35}$$

The corresponding growth rate is

$$\boxed{\gamma_{\max}\tau_{A,a} \sim S_a^{-1/2}, \qquad \gamma_{\max} \sim v_A^{1/2}\bar\eta^{1/2}a^{-3/2}.} \tag{4.36}$$

These wavenumber scalings use the Harris-sheet form of $\Delta'(k)$. The mode must also fit into a finite sheet: roughly $k_{\max}L \gtrsim 1$. The calculation requires a collisional fluid description of the inner layer and negligible viscous effects; it is not a collisionless-tearing result.

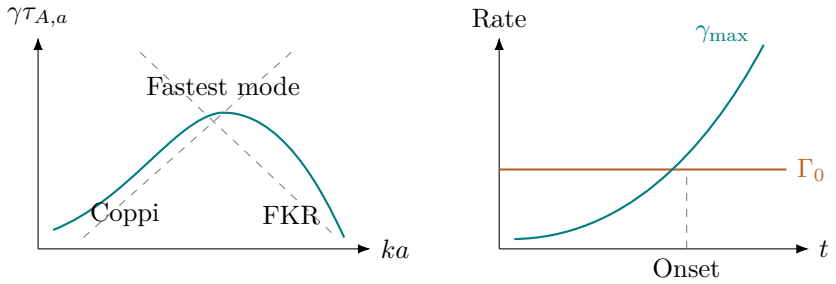


Figure 9: Two comparisons that organize the tearing problem. Left: the tearing spectrum has a fastest-growing mode between the indicated branches. Right: as the sheet thins, tearing can overtake the imposed sheet-formation rate. Curves are qualitative.

4.9 Onset in a forming sheet

Initially the configuration evolves mainly through the ideal flow: the current layer narrows while the tearing perturbation remains weak. At fixed v_A and $\bar\eta$, equation (4.36) gives $\gamma_{\max} \propto a^{-3/2}$, so thinning makes tearing faster. Comparing $\gamma_{\max}$ with the sheet-formation rate Γ_0 identifies when tearing can compete with the changing background, as in figure 9. Actual disruption also depends on the initial perturbation amplitude and the growth accumulated during sheet formation [5].

The result is a linear instability growth rate. It is not yet a prediction of the nonlinear reconnection rate. The subsequent nonlinear tearing stage, saturation, and X-point collapse are left for further reading [8, 9, 10, 11]. We next develop the steady Sweet–Parker model, whose thickness will let us apply the tearing result to the plasmoid instability.

5 The Sweet–Parker model

From this section onward, $\boldsymbol{B}$ and the flux function ψ again denote physical magnetic fields and fluxes. The conversion is $\psi_{\text{physical}} = \sqrt{4\pi\rho_0}\,\psi_{\text{RMHD}}$; velocities and magnetic diffusivity $\bar{\eta}$ are unchanged.

5.1 Geometry and assumptions

The Sweet–Parker model is a two-dimensional, steady, resistive-MHD model of a long, thin reconnection layer [12, 13]. Let δ be the thickness scale of the current sheet and L its length scale, with $L/\delta \gg 1$. The upstream magnetic field is B_{in}, the inflow speed is u_{in}, and the outflow speed is u_{out}. The field changes across the sheet over δ. Factors of two from using full widths or half-widths do not affect the scaling.

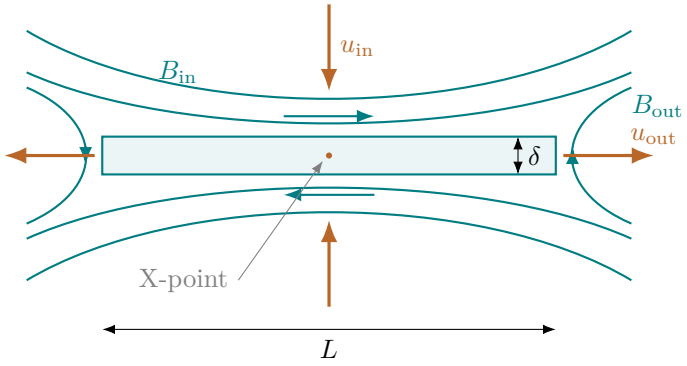


Figure 10: The Sweet–Parker geometry. Plasma and magnetic flux enter across the long sides; accelerated plasma leaves through the short ends.

5.2 Match the electric field outside and inside the sheet

Far from the sheet, the current is small enough that the resistive term in Ohm's law is negligible. In magnitude,

$$E_{\text{away}} \sim \frac{u_{\text{in}} B_{\text{in}}}{c}. \tag{5.1}$$

Near the X-point, the reconnecting field is small and the non-ideal term supplies the electric field:

$$E_{\text{CS}} \sim \eta j_z, \qquad j_z \sim \frac{c}{4\pi}\frac{B_{\text{in}}}{\delta}. \tag{5.2}$$

For a steady magnetic field, Faraday's law gives $\boldsymbol{\nabla} \times \boldsymbol{E} = 0$. In two dimensions, $\partial_z = 0$, its in-plane components imply

$$\partial_x E_z = \partial_y E_z = 0.$$

Thus the reconnecting component E_z is spatially uniform. Matching its magnitude between the upstream region and the current sheet,

$$\frac{u_{\text{in}} B_{\text{in}}}{c} \sim \eta \frac{c}{4\pi}\frac{B_{\text{in}}}{\delta} \quad \Longrightarrow \quad \boxed{u_{\text{in}} \sim \frac{\bar{\eta}}{\delta}.} \tag{5.3}$$

This relation uses electrical resistivity in Ohm's law and magnetic diffusivity in the final expression.

5.3 Incompressibility and the outflow speed

For incompressible flow, $\boldsymbol{\nabla} \cdot \boldsymbol{u} = 0$, conservation of mass gives

$$u_{\text{in}} L \sim u_{\text{out}} \delta, \qquad \boxed{\frac{u_{\text{in}}}{\delta} \sim \frac{u_{\text{out}}}{L}.} \tag{5.4}$$

The momentum equation has not yet been used. For an energetic estimate, compare the upstream magnetic energy density with the outflow kinetic energy density:

$$\frac{B_{\rm in}^2}{8\pi} \sim \frac{1}{2}\rho u_{\rm out}^2 \quad \Longrightarrow \quad \boxed{u_{\rm out} \sim \frac{B_{\rm in}}{\sqrt{4\pi\rho}} \equiv v_A.} \tag{5.5}$$

This is a scaling estimate for an Alfvénic outflow, not a statement that all magnetic energy becomes bulk kinetic energy.

Combine equations (5.3)–(5.5):

$$\delta \sim \frac{u_{\rm in}}{v_A} L \sim \frac{\bar{\eta}}{u_{\rm in}}, \qquad u_{\rm in}^2 \sim \frac{\bar{\eta} v_A}{L} = \frac{v_A^2}{S}.$$

Therefore

$$\boxed{\frac{u_{\rm in}}{v_A} \sim \frac{\delta}{L} \sim S^{-1/2}, \qquad S = \frac{L v_A}{\bar{\eta}}.} \tag{5.6}$$

5.4 Flux-transfer rate and reconnection time

For a two-dimensional system, write ψ for the magnetic flux per unit length in the ignorable direction. The field contained across the sheet has a flux scale $B_{\rm in}\delta$, and the associated inflow time is $\delta/u_{\rm in}$. Thus

$$\left|\frac{{\rm d}\psi}{{\rm d}t}\right| \sim \frac{B_{\rm in}\delta}{\delta/u_{\rm in}} \sim B_{\rm in} u_{\rm in}. \tag{5.7}$$

The flux-transfer rate is directly related to the reconnection electric field:

$$\boxed{\left|\frac{{\rm d}\psi}{{\rm d}t}\right| = c|E_z| \sim B_{\rm in} u_{\rm in}.} \tag{5.8}$$

The normalized reconnection rate is consequently

$$\boxed{\epsilon_{\rm rec} \equiv \frac{c|E_z|}{v_A B_{\rm in}} \sim \frac{B_{\rm in} u_{\rm in}}{v_A B_{\rm in}} \sim \frac{u_{\rm in}}{v_A} \sim S^{-1/2}.} \tag{5.9}$$

The normalization also has a macroscopic interpretation. A system of characteristic extent L contains flux per unit length of order $\psi_L \sim L B_{\rm in}$. Its reconnection time is

$$\begin{aligned} \tau_{\rm rec} &\sim \frac{\psi_L}{|{\rm d}\psi/{\rm d}t|} \sim \frac{L B_{\rm in}}{B_{\rm in} u_{\rm in}} \sim \frac{L}{u_{\rm in}} \\ &\sim \frac{L}{v_A} S^{1/2} = \tau_{A,L} S^{1/2}. \end{aligned} \tag{5.10}$$

Equivalently,

$$\boxed{\frac{\tau_{A,L}}{\tau_{\rm rec}} \sim S^{-1/2} \sim \epsilon_{\rm rec}.} \tag{5.11}$$

The normalized rate measures how much slower the flux is processed than on a macroscopic Alfvén time.

5.5 Is the Sweet–Parker rate fast enough?

At very large S, equation (5.6) gives a small inflow and a long reconnection time. For example, take $\tau_{A,L} \sim 1\,\mathrm{s}$ and $S^{1/2} \sim 10^6$, giving $\tau_{\mathrm{rec}} \sim 10^6\,\mathrm{s}$, or about twelve days. This is far longer than the rapid solar-flare evolution motivating the discussion.

The Petschek model offers another possibility: a short diffusion region and attached slow shocks can produce a much faster rate [14]. Establishing that geometry requires additional physics or conditions beyond the Sweet–Parker assumptions. We do not develop the shock solution here. Instead, we first examine evidence for Sweet–Parker reconnection and then ask whether its long, thin current sheet remains stable.

6 Sweet–Parker reconnection in simulations and experiments

The Sweet–Parker model provides a concrete resistive-MHD benchmark. Its prediction is

$$\epsilon_{\mathrm{rec}} \equiv \frac{c|E_z|}{v_A B_{\mathrm{in}}} \sim \frac{u_{\mathrm{in}}}{v_A} \sim S^{-1/2}, \qquad S = \frac{L v_A}{\bar{\eta}}. \tag{6.1}$$

The square-root dependence on resistivity is seen in resistive-MHD calculations of the reconnection stage following current-sheet formation [11]. The Magnetic Reconnection Experiment (MRX) also provides a laboratory test: measured inflow speeds agree with Sweet–Parker scaling when the appropriate effective Lundquist number is used [15]. These examples establish the model's relevance within its regime of validity. The next question is whether a long, thin Sweet–Parker sheet can remain stable as S becomes large.

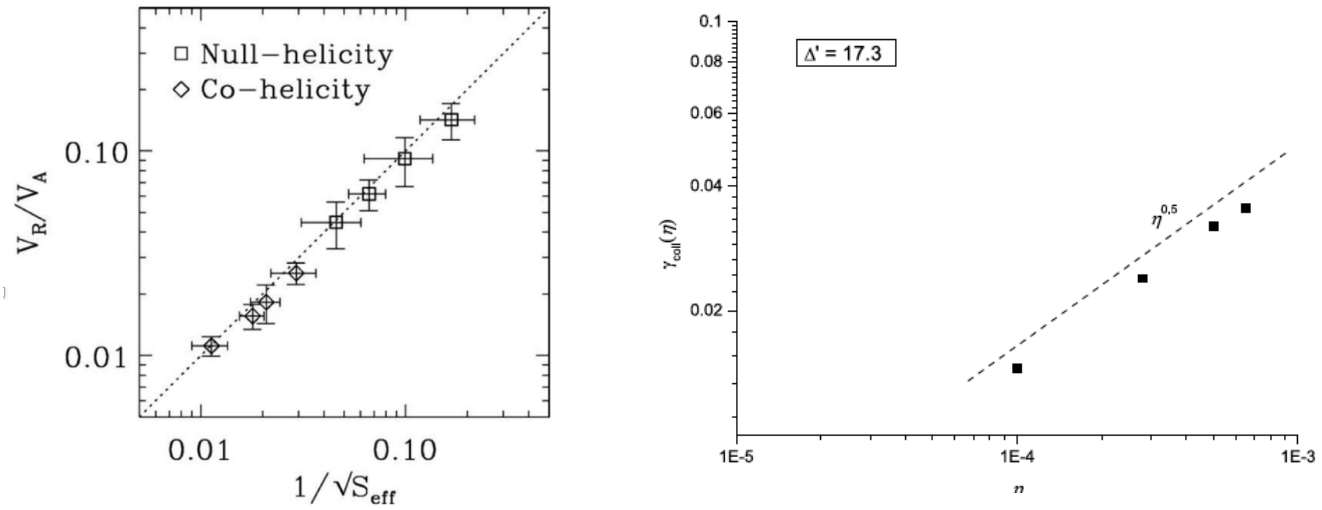


Figure 11: Tests of Sweet–Parker scaling. Left: MRX inflow speed versus $1/\sqrt{S_{\mathrm{eff}}}$ [15]. Right: the square-root resistivity dependence in a resistive-MHD calculation [11].

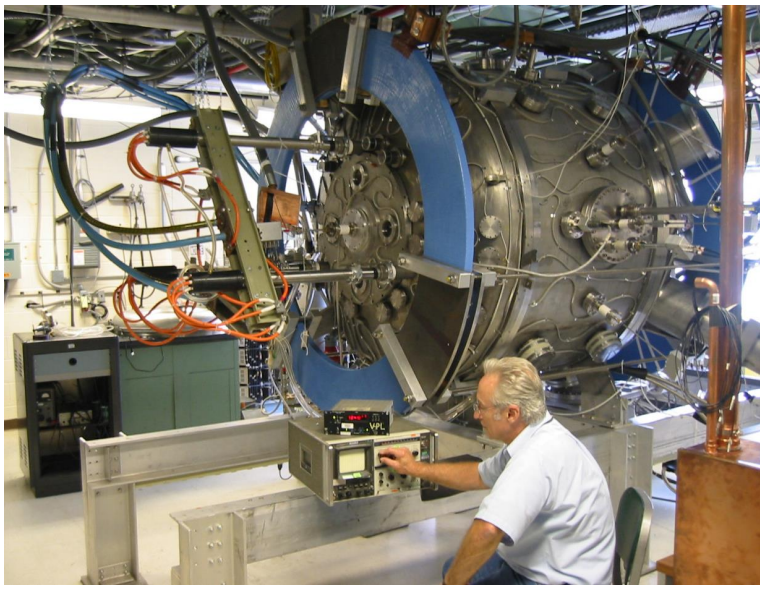


Figure 12: The MRX apparatus at the Princeton Plasma Physics Laboratory, where reconnection can be studied under controlled laboratory conditions. Image: PPPL/MRX.

7 Is the Sweet–Parker current sheet stable?

A current sheet can form as an X-point collapses during nonlinear island evolution [11]. The resulting elongated sheet provides the setting for the secondary instability discussed next.

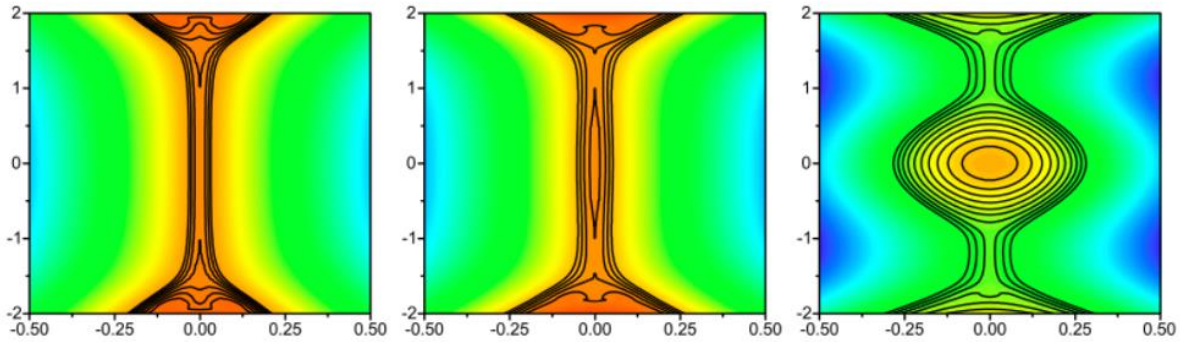


Figure 13: Magnetic configurations during nonlinear island evolution: an elongated current sheet can itself develop a secondary island [11].

7.1 The plasmoid instability

At sufficiently large S, the Sweet–Parker current sheet is unstable to a tearing-like instability that produces many magnetic islands, or *plasmoids* [16, 17, 18]. Thus a single elongated reconnection layer need not remain a single sheet.

Applying tearing theory to a Sweet–Parker-type configuration gives the fastest-growing mode scalings [18, 19]

$$\gamma_{\max}\tau_{A,\mathrm{CS}} \sim S^{1/4}, \qquad k_{\max}L_{\mathrm{CS}} \sim S^{3/8}, \tag{7.1}$$

$$\tau_{A,\mathrm{CS}} = \frac{L_{\mathrm{CS}}}{v_A}, \qquad S = \frac{L_{\mathrm{CS}}v_A}{\bar{\eta}}. \tag{7.2}$$

The striking feature is that the growth rate becomes *faster* relative to the global Alfvén crossing rate

as S increases. The number of plasmoids also increases. A commonly encountered onset threshold in resistive-MHD simulations is $S \gtrsim 10^4$; its precise value depends on the current-sheet configuration and other parameters.

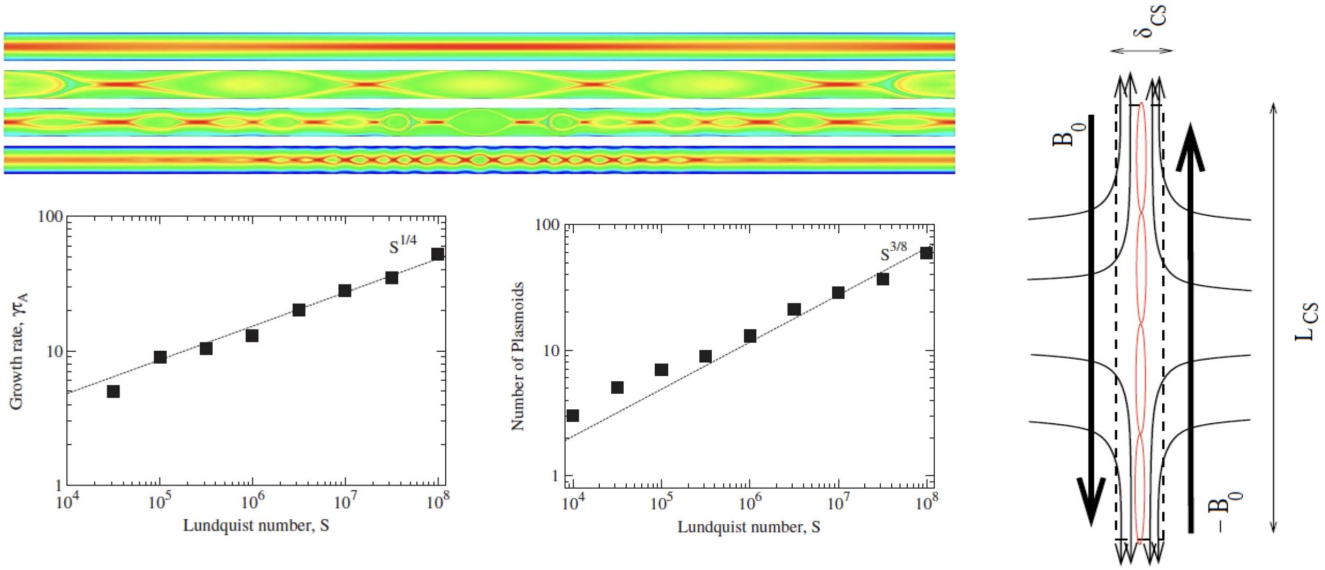


Figure 14: Tearing of a Sweet–Parker current sheet. Right: current-sheet geometry. Upper left: increasing S from 10^4 to 10^7 produces progressively more plasmoids. Lower left: numerical growth rates and plasmoid numbers follow the $S^{1/4}$ and $S^{3/8}$ scalings [18, 20].

7.2 The nonlinear regime: hierarchical plasmoid chains

The nonlinear layer contains plasmoids separated by shorter current sheets. Those sheets can themselves become unstable, producing a hierarchy of islands and reconnecting layers [17, 21]. The resulting configuration is dynamic: plasmoids form, interact, grow, and leave the layer.

In the nonlinear statistical steady state, the reconnection rate becomes approximately independent of resistivity over the plasmoid-dominated regime, with a characteristic value

$$\epsilon_{\rm rec} \sim 0.01 \tag{7.3}$$

for the resistive-MHD conditions illustrated here [22, 23]. This is a substantial change from the $S^{-1/2}$ Sweet–Parker prediction.

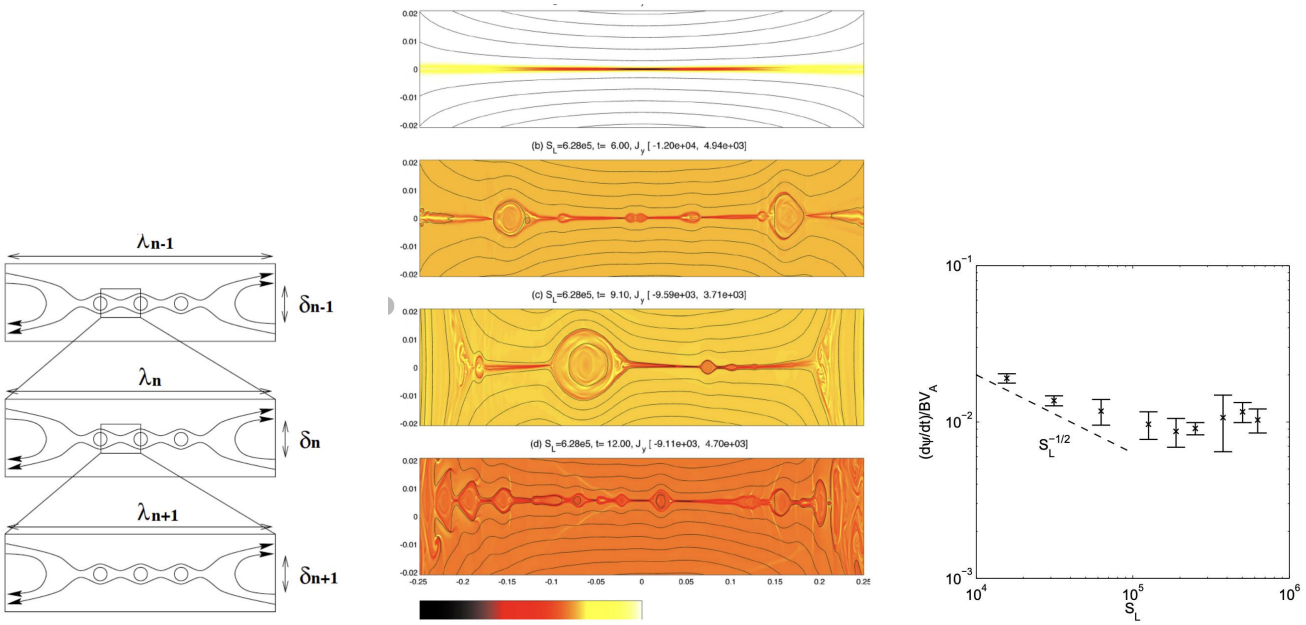


Figure 15: Nonlinear plasmoid reconnection. Left: hierarchical fragmentation of current sheets [17]. Middle: the evolution of a plasmoid chain [21]. Right: the reconnection rate becomes nearly independent of S, rather than following the dashed Sweet–Parker scaling [22].

8 Plasmoids in the laboratory, the Sun, and astrophysical systems

8.1 Laboratory and solar examples

Plasmoid formation is not confined to numerical calculations. Laboratory experiments produce reconnecting plasma flows and resolve structures within the current layer [24]. Solar observations also show small structures associated with reconnecting layers [25]. These examples connect the current-sheet instability to systems with very different sizes and plasma parameters. The FLARE experiment at PPPL is another laboratory platform intended to explore reconnection in large, multiscale current sheets.

8.2 Consequences of plasmoid formation

Plasmoids change the magnetic geometry and the ways in which particles gain energy. Particles can become trapped in islands and be accelerated as the islands evolve [26]. In three dimensions, instabilities and the interaction of magnetic structures produce complex, turbulent reconnection dynamics [27]. Plasmoid formation can also affect the global dynamics of an accretion flow [28].

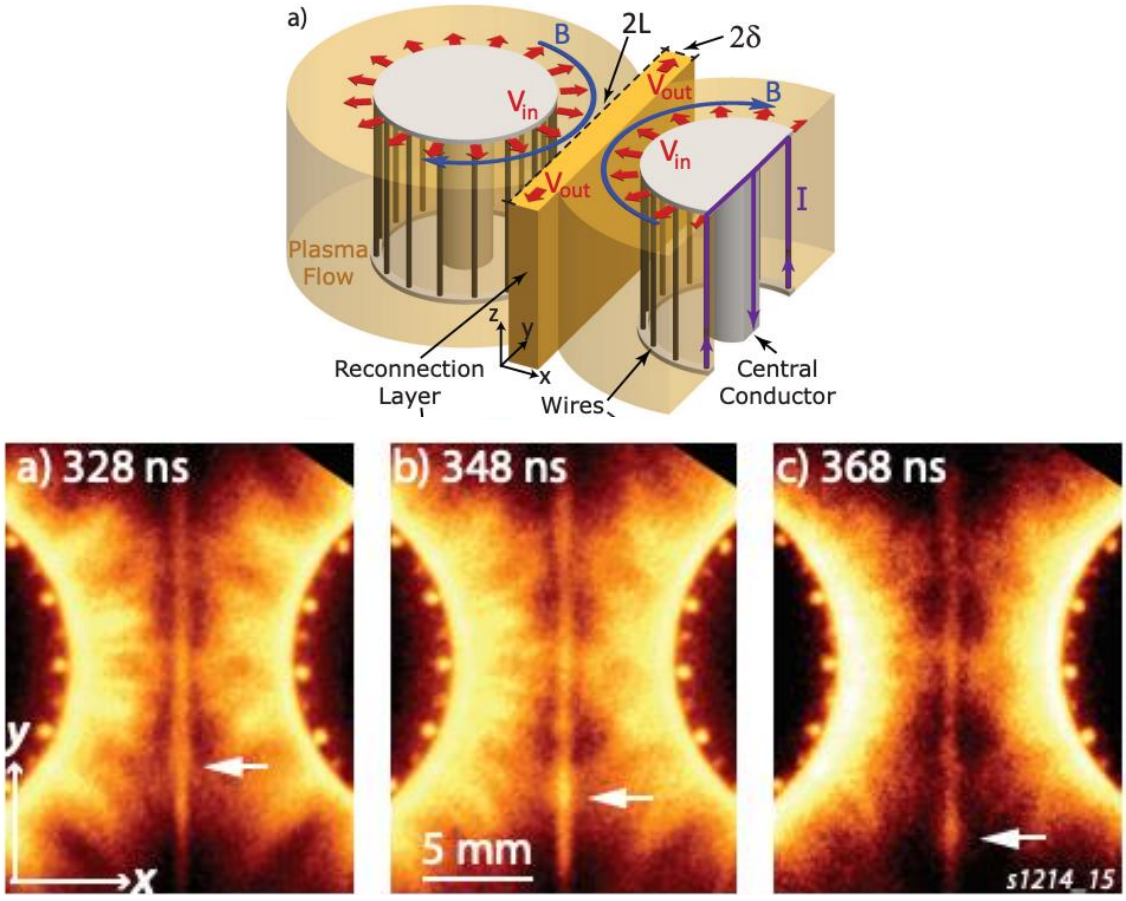


Figure 16: A laboratory reconnection experiment. The setup drives two magnetized plasma flows into a reconnecting layer; the image sequence shows the layer and an evolving plasmoid, indicated by the arrows [24].

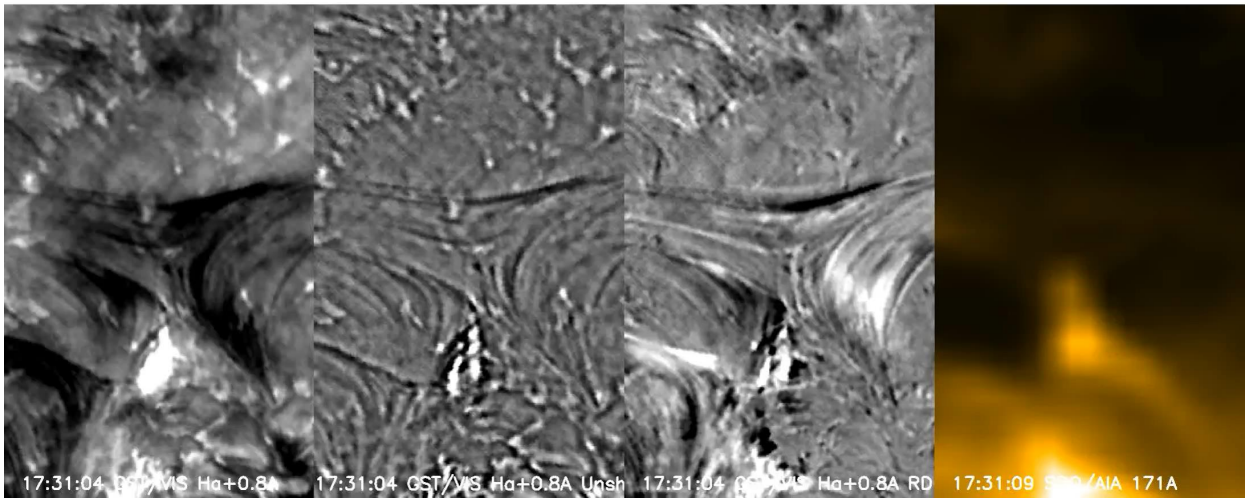


Figure 17: A solar reconnection example observed in Hα and the 171 Å channel. The different views resolve the reconnecting structure and its surroundings [25].

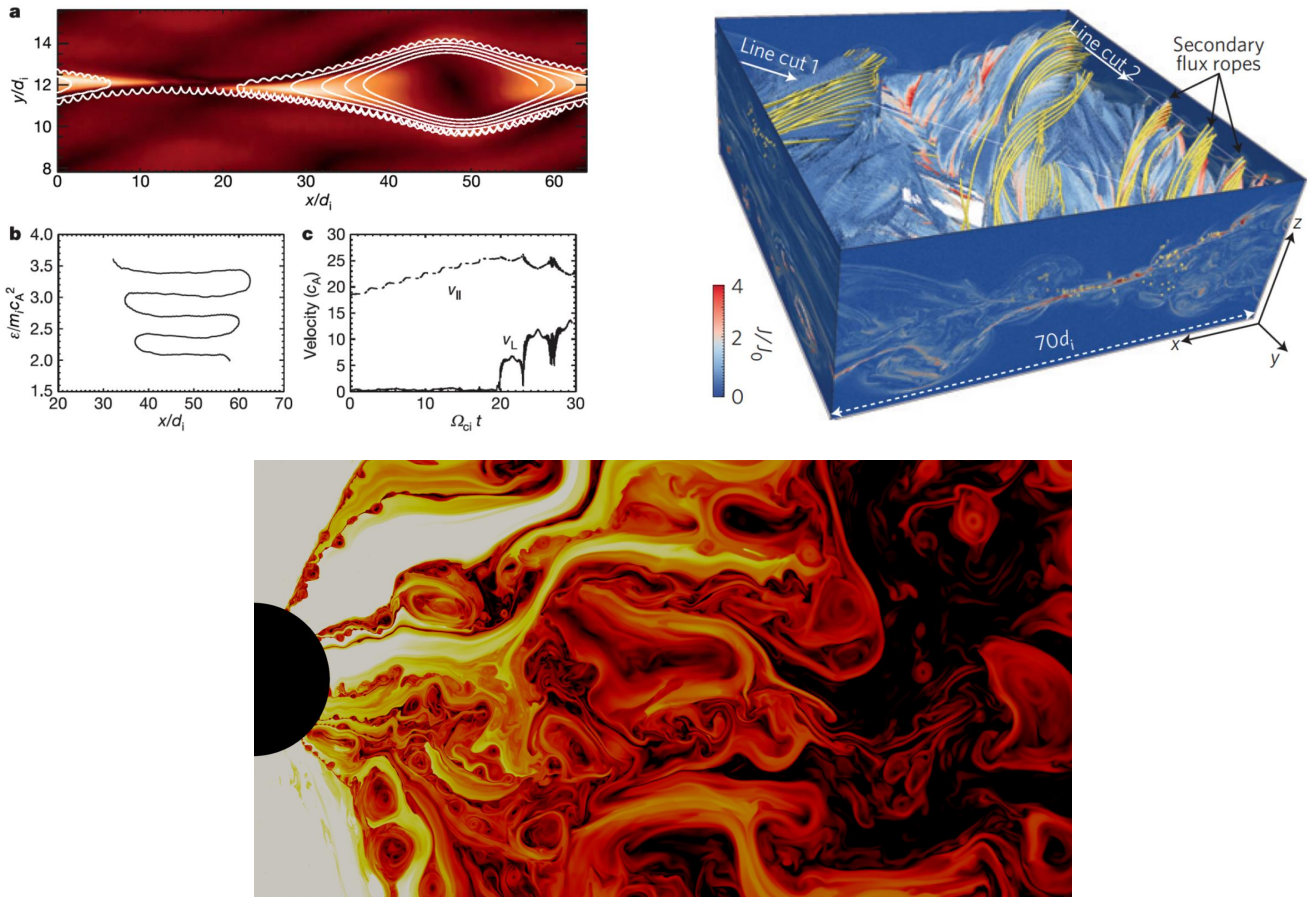


Figure 18: Consequences of plasmoid dynamics. Upper left: a trapped particle and its energization in an evolving island [26]. Upper right: three-dimensional reconnection with complex magnetic structures [27]. Bottom: an accretion-flow example (image: B. Ripperda); see [28, 29] for related simulations.

9 Collisionless reconnection

When a current sheet approaches ion and electron kinetic scales, resistive MHD is no longer sufficient to describe its internal structure. The generalized Ohm's law identifies the additional terms:

$$\mathbf{E} + \frac{\mathbf{v}_i \times \mathbf{B}}{c} = \eta \mathbf{j} + \frac{\mathbf{j} \times \mathbf{B}}{nec} - \frac{1}{ne} \nabla \cdot \mathbf{P}_e - \frac{m_e}{e} \frac{D_e \mathbf{v}_e}{Dt}, \qquad \frac{D_e}{Dt} = \frac{\partial}{\partial t} + \mathbf{v}_e \cdot \nabla. \tag{9.1}$$

Here $\mathbf{v}_i$ and $\mathbf{v}_e$ are the ion and electron bulk velocities, n is their common number density, e is the positive elementary charge, and $\mathbf{P}_e$ is the electron pressure tensor. The current $\mathbf{j}$ is the physical electric current density, and η is the electrical resistivity.

The Hall term, $\mathbf{j} \times \mathbf{B}/(nec)$, distinguishes ion motion from electron motion, with the ion inertial scale $d_i = c/\omega_{pi}$ entering the dynamics. The electron pressure tensor and electron inertia become important at smaller scales; the electron inertial scale is $d_e = c/\omega_{pe}$. The ion-sound gyroradius ρ_s is another characteristic scale. Relevant dispersive wave responses include whistler and kinetic Alfvén waves.

The Hall term alone does not break magnetic flux freezing into the electron flow: it changes which fluid carries the field. Electron pressure-tensor effects and electron inertia can support the electric field that breaks electron flux freezing. These effects should therefore not all be represented as a scalar "effective resistivity."

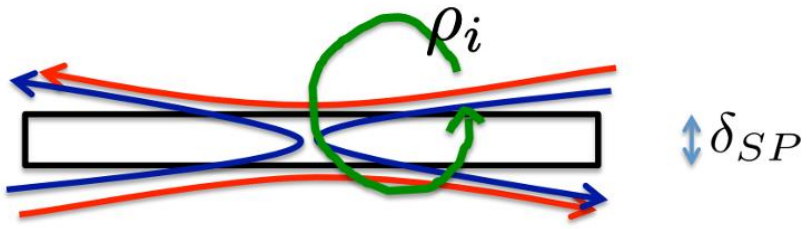


Figure 19: The MHD description of the layer must be reconsidered when its thickness is comparable to a particle orbit scale. The sketch compares an ion gyroradius ρ_i with the Sweet–Parker thickness δ_{SP}.

A normalized reconnection rate of order

$$\epsilon_{\mathrm{rec}} \sim 0.1 \tag{9.2}$$

is common in collisionless reconnection. Understanding why this value appears across many configurations, and how it depends on the plasma conditions and geometry, is an important part of reconnection research [30, 31].

10 Challenges and astrophysical applications

10.1 Why the problem remains difficult

Reconnection is intrinsically multiscale: microscopic physics changes field connectivity within a thin layer, while the inflow, outflow, and energy release involve much larger regions. The dynamics are often time dependent, even when time-averaged rates can be defined. The wide range of plasma conditions and magnetic geometries makes it difficult for a single simplified model to capture every reconnection environment.

10.2 Particle acceleration, radiation, and black-hole environments

Reconnection can efficiently produce nonthermal particles. Kinetic simulations demonstrate the development of broad particle-energy distributions as magnetic energy is released [32]. Radiative cooling adds

another channel to the energy budget and can modify the reconnecting plasma; both two-dimensional kinetic studies and three-dimensional radiative calculations explore this coupling [33, 34].

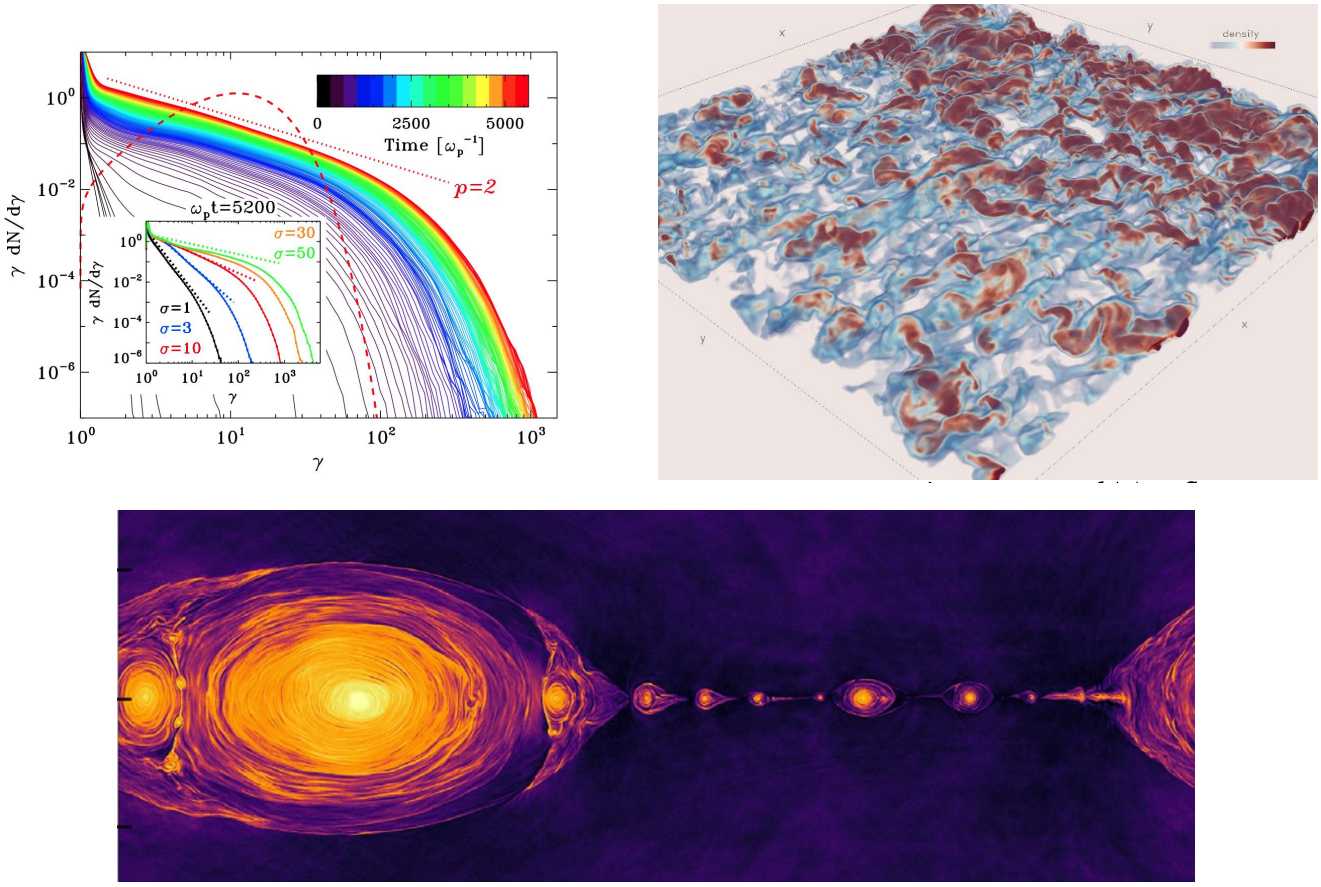


Figure 20: Kinetic and radiative reconnection. Upper left: the development of nonthermal particle-energy distributions [32]. Upper right: three-dimensional reconnection with radiative cooling [34]. Bottom: structure in a radiative kinetic reconnection calculation [33].

Black-hole environments provide a setting where reconnection, particle acceleration, and radiation are closely connected. Reconnecting structures arise in simulations of black-hole magnetospheres [35], and reconnection-powered particle acceleration is a proposed source of TeV flares [36].

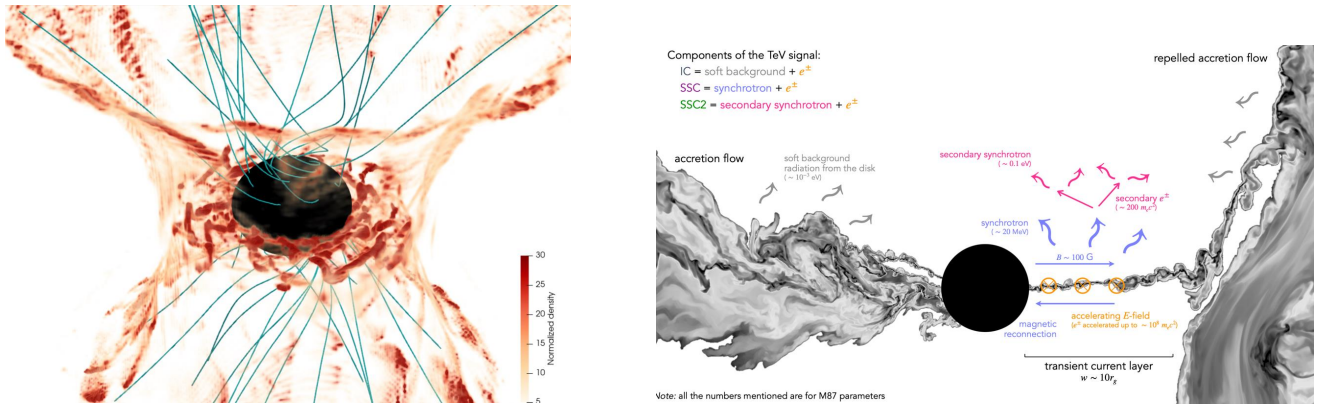


Figure 21: Reconnection near black holes. Left: magnetic structures in a black-hole magnetosphere calculation [35]. Right: an example of how reconnection-powered particle acceleration can contribute to TeV emission [36].

11 The interaction between reconnection and turbulence

11.1 Reconnection in a turbulent background

Turbulence changes the geometry of a reconnecting layer. In the field-line-wandering picture, the width through which plasma leaves the layer is controlled by the wandering of magnetic field lines, rather than solely by the resistive Sweet–Parker thickness [37]. A broader outflow region permits a faster reconnection rate.

Numerical calculations with a turbulent background show rates of order 0.1 for the parameters illustrated here, with much weaker resistivity dependence than the corresponding laminar Sweet–Parker case [38]. This numerical value is an example, rather than a universal rate independent of the turbulence strength and geometry.

11.2 Reconnection-mediated turbulence

The influence also runs in the opposite direction. Turbulence generates thin current sheets. If tearing disrupts those sheets before the turbulent cascade transfers their energy onward, reconnection becomes part of the cascade dynamics and can change the turbulent spectrum [39, 40].

Large simulations show plasmoids within turbulent current sheets and a change in spectral behavior associated with reconnection [41, 42]. The key connection is that reconnection and turbulence need not be treated as separate processes: turbulence creates the structures that reconnect, and reconnection changes the subsequent transfer of energy.

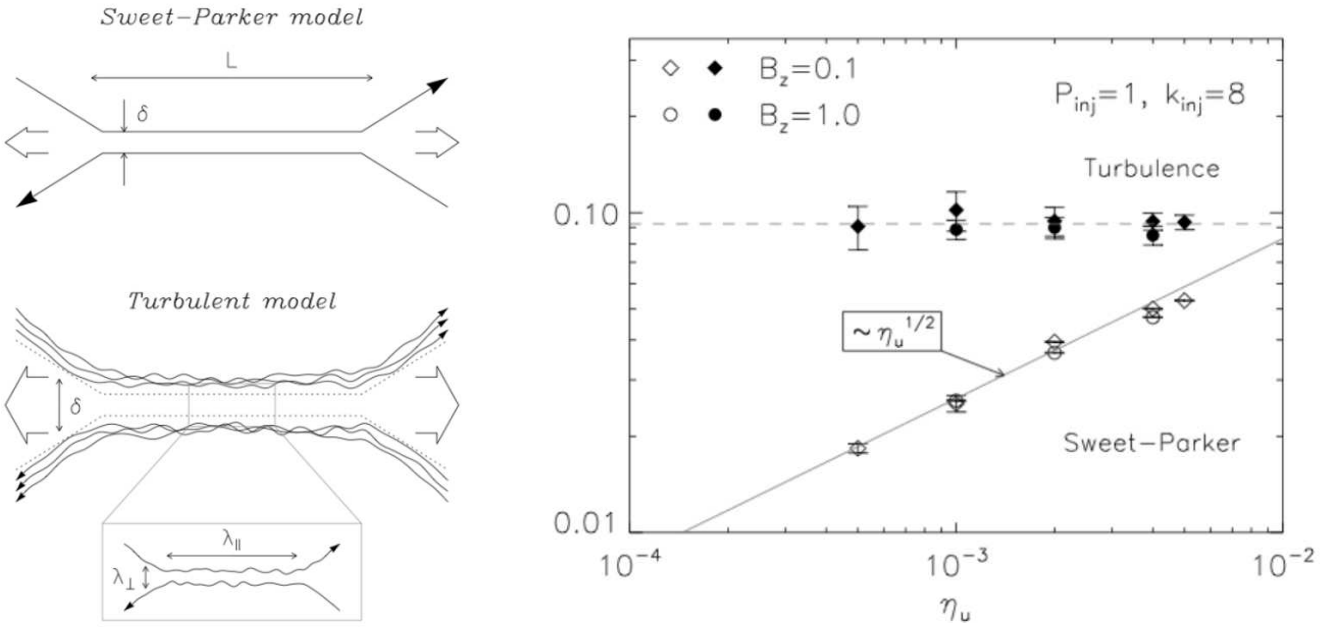


Figure 22: Reconnection in a turbulent background. Left: the comparison between a Sweet–Parker layer and a layer broadened by field-line wandering [37]. Right: numerical reconnection rates with and without background turbulence [38].

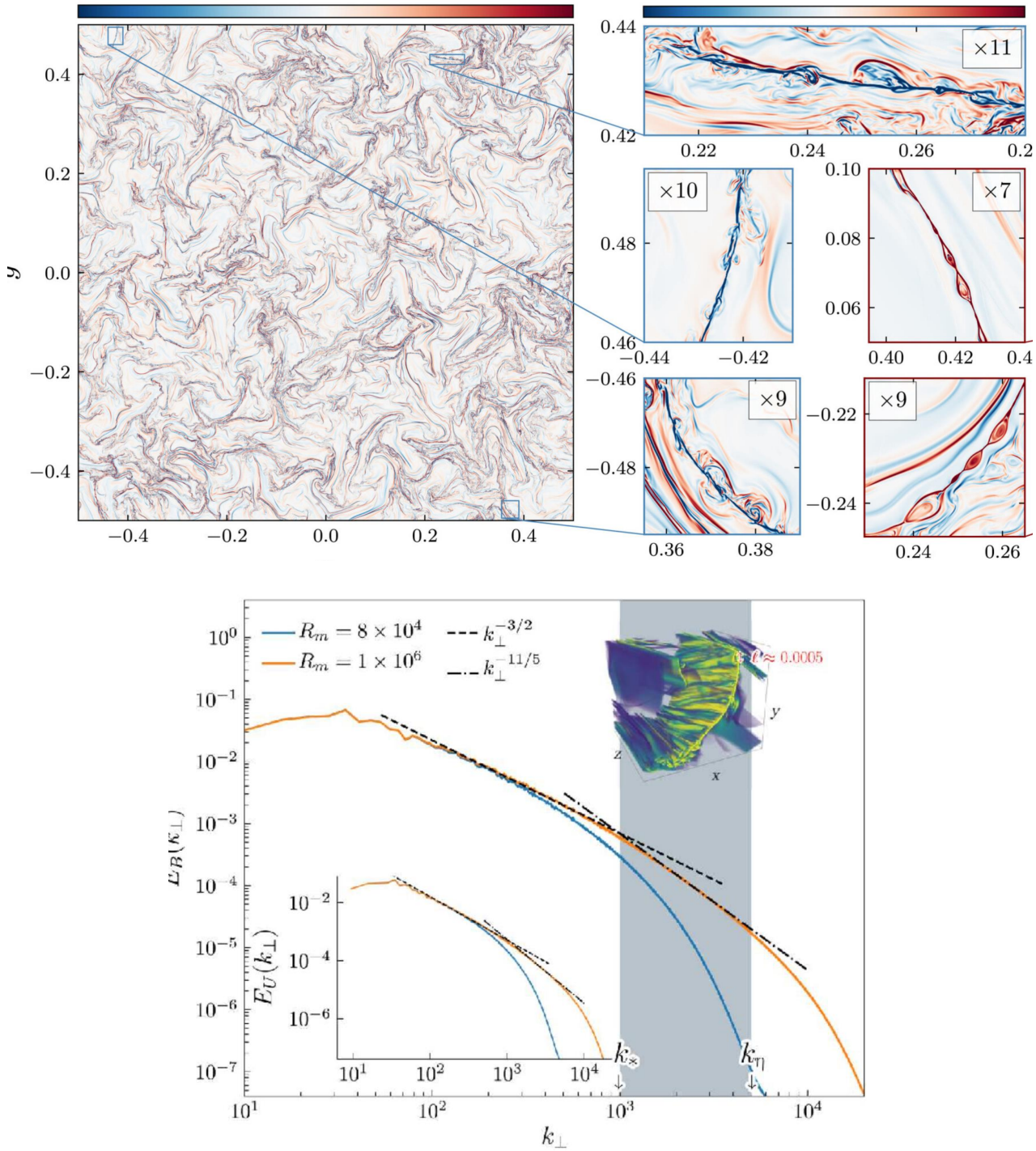


Figure 23: Reconnection within turbulence. Top: current sheets and plasmoid-containing structures revealed by successive enlargements [41]. Bottom: an example of a spectral change associated with a reconnection-mediated range in a high-resolution calculation [42].

References

[1] L. Fletcher et al. (2011), *An Observational Overview of Solar Flares*, Space Science Reviews **159**, 19–106. 10.1007/s11214-010-9701-8. See Sections 1 and 7.1.1 for rapid energy release and magnetic-energy storage; open-access version.

[2] NASA Scientific Visualization Studio (2011), *SDO EVE Late Phase Flares*. Original animation, still image, and explanations. The multi-panel visual with AIA, HMI, and EVE is the direct source of figure 1 and its panel identifications.

[3] T. N. Woods et al. (2011), *New Solar Extreme-Ultraviolet Irradiance Observations During Flares*, The Astrophysical Journal **739**, 59. 10.1088/0004-637X/739/2/59. Observational interpretation of the EVE light curves and EUV late phase, including the 2010 May 5 event; open-access article.

[4] M. Yamada, F. M. Levinton, N. Pomphrey, R. Budny, J. Manickam, and Y. Nagayama (1994), *Investigation of magnetic reconnection during a sawtooth crash in a high-temperature tokamak plasma*, Physics of Plasmas **1**, 3269–3276. DOI.

[5] E. A. Tolman, N. F. Loureiro, and D. A. Uzdensky (2018), *Development of tearing instability in a current sheet forming by sheared incompressible flow*, Journal of Plasma Physics **84**, 905840115. DOI.

[6] B. Coppi, R. Galvão, R. Pellat, M. N. Rosenbluth, and P. H. Rutherford (1976), *Resistive internal kink modes*, Fizika Plazmy **2**, 961–966 [Soviet Journal of Plasma Physics **2**, 533]. Author report.

[7] H. P. Furth, J. Killeen, and M. N. Rosenbluth (1963), *Finite-Resistivity Instabilities of a Sheet Pinch*, Physics of Fluids **6**, 459–484. DOI.

[8] P. H. Rutherford (1973), *Nonlinear growth of the tearing mode*, Physics of Fluids **16**, 1903–1908. DOI.

[9] F. Militello and F. Porcelli (2004), *Simple analysis of the nonlinear saturation of the tearing mode*, Physics of Plasmas **11**, L13–L16. DOI.

[10] D. F. Escande and M. Ottaviani (2004), *Simple and rigorous solution for the nonlinear tearing mode*, Physics Letters A **323**, 278–284. DOI.

[11] N. F. Loureiro, S. C. Cowley, W. D. Dorland, M. G. Haines, and A. A. Schekochihin (2005), *X-Point Collapse and Saturation in the Nonlinear Tearing Mode Reconnection*, Physical Review Letters **95**, 235003. DOI.

[12] P. A. Sweet (1958), *The neutral point theory of solar flares*, in *Electromagnetic Phenomena in Cosmical Physics*, IAU Symposium **6**, edited by B. Lehnert, pp. 123–134. DOI.

[13] E. N. Parker (1957), *Sweet's mechanism for merging magnetic fields in conducting fluids*, Journal of Geophysical Research **62**, 509–520. DOI.

[14] H. E. Petschek (1964), *Magnetic Field Annihilation*, in *The Physics of Solar Flares*, edited by W. N. Hess, NASA SP-50, pp. 425–439.

[15] H. Ji, M. Yamada, S. Hsu, R. Kulsrud, T. Carter, and S. Zaharia (1999), *Magnetic reconnection with Sweet-Parker characteristics in two-dimensional laboratory plasmas*, Physics of Plasmas **6**, 1743–1750. DOI.

[16] D. Biskamp (1986), *Magnetic reconnection via current sheets*, Physics of Fluids **29**, 1520–1531. DOI.

[17] K. Shibata and S. Tanuma (2001), *Plasmoid-induced-reconnection and fractal reconnection*, Earth, Planets and Space **53**, 473–482. DOI.

[18] N. F. Loureiro, A. A. Schekochihin, and S. C. Cowley (2007), *Instability of current sheets and formation of plasmoid chains*, Physics of Plasmas **14**, 100703. DOI.

[19] N. F. Loureiro, A. A. Schekochihin, and D. A. Uzdensky (2013), *Plasmoid and Kelvin–Helmholtz instabilities in Sweet–Parker current sheets*, Physical Review E **87**, 013102. DOI.

[20] R. Samtaney, N. F. Loureiro, D. A. Uzdensky, A. A. Schekochihin, and S. C. Cowley (2009), *Formation of Plasmoid Chains in Magnetic Reconnection*, Physical Review Letters **103**, 105004. DOI.

[21] Y.-M. Huang and A. Bhattacharjee (2012), *Distribution of Plasmoids in High-Lundquist-Number Magnetic Reconnection*, Physical Review Letters **109**, 265002. DOI.

[22] A. Bhattacharjee, Y.-M. Huang, H. Yang, and B. Rogers (2009), *Fast reconnection in high-Lundquist-number plasmas due to the plasmoid instability*, Physics of Plasmas **16**, 112102. DOI.

[23] D. A. Uzdensky, N. F. Loureiro, and A. A. Schekochihin (2010), *Fast Magnetic Reconnection in the Plasmoid-Dominated Regime*, Physical Review Letters **105**, 235002. DOI.

[24] J. D. Hare et al. (2017), *Anomalous Heating and Plasmoid Formation in a Driven Magnetic Reconnection Experiment*, Physical Review Letters **118**, 085001. DOI.

[25] G. Cheng, L. Ni, Z. Tang, Y. Chen, Y. Chen, J. Hu, and J. Lin (2024), *Evidence for Plasmoid-mediated Magnetic Reconnection during a Small-scale Flare in the Partially Ionized Low Solar Atmosphere*, Astrophysical Journal Letters **966**, L29. DOI.

[26] J. F. Drake, M. Swisdak, H. Che, and M. A. Shay (2006), *Electron acceleration from contracting magnetic islands during reconnection*, Nature **443**, 553–556. DOI.

[27] W. Daughton, V. Roytershteyn, H. Karimabadi, L. Yin, B. J. Albright, B. Bergen, and K. J. Bowers (2011), *Role of electron physics in the development of turbulent magnetic reconnection in collisionless plasmas*, Nature Physics **7**, 539–542. DOI.

[28] B. Ripperda et al. (2019), *General-relativistic Resistive Magnetohydrodynamics with Robust Primitive-variable Recovery for Accretion Disk Simulations*, Astrophysical Journal Supplement Series **244**, 10. DOI.

[29] B. Ripperda, F. Bacchini, and A. A. Philippov (2020), *Magnetic Reconnection and Hot Spot Formation in Black Hole Accretion Disks*, Astrophysical Journal **900**, 100. DOI.

[30] Y.-H. Liu, M. Hesse, F. Guo, W. Daughton, H. Li, P. A. Cassak, and M. A. Shay (2017), *Why Does Steady-State Magnetic Reconnection Have a Maximum Local Rate of Order 0.1?*, Physical Review Letters **118**, 085101. DOI.

[31] P. A. Cassak, Y.-H. Liu, and M. A. Shay (2017), *A review of the 0.1 reconnection rate problem*, Journal of Plasma Physics **83**, 715830501. DOI.

[32] L. Sironi and A. Spitkovsky (2014), *Relativistic Reconnection: An Efficient Source of Non-thermal Particles*, Astrophysical Journal Letters **783**, L21. DOI.

[33] G. R. Werner, A. A. Philippov, and D. A. Uzdensky (2019), *Particle acceleration in relativistic magnetic reconnection with strong inverse-Compton cooling in pair plasmas*, Monthly Notices of the Royal Astronomical Society: Letters **482**, L60–L64. DOI.

[34] A. Chernoglazov, H. Hakobyan, and A. A. Philippov (2023), *High-energy Radiation and Ion Acceleration in Three-dimensional Relativistic Magnetic Reconnection with Strong Synchrotron Cooling*, Astrophysical Journal **959**, 122. DOI.

[35] B. Crinquand, B. Cerutti, G. Dubus, K. Parfrey, and A. A. Philippov (2022), *Images of Magnetospheric Reconnection-Powered Radiation around Supermassive Black Holes*, Physical Review Letters **129**, 205101. DOI.

[36] H. Hakobyan, B. Ripperda, and A. A. Philippov (2023), *Radiative Reconnection-powered TeV Flares from the Black Hole Magnetosphere in M87*, Astrophysical Journal Letters **943**, L29. DOI.

[37] A. Lazarian and E. T. Vishniac (1999), *Reconnection in a Weakly Stochastic Field*, Astrophysical Journal **517**, 700–718. DOI.

[38] G. Kowal, A. Lazarian, E. T. Vishniac, and K. Otmianowska-Mazur (2009), *Numerical Tests of Fast Reconnection in Weakly Stochastic Magnetic Fields*, Astrophysical Journal **700**, 63–85. DOI.

[39] N. F. Loureiro and S. Boldyrev (2017), *Role of Magnetic Reconnection in Magnetohydrodynamic Turbulence*, Physical Review Letters **118**, 245101. DOI.

[40] A. Mallet, A. A. Schekochihin, and B. D. G. Chandran (2017), *Disruption of sheet-like structures in Alfvénic turbulence by magnetic reconnection*, Monthly Notices of the Royal Astronomical Society **468**, 4862–4871. DOI.

[41] C. Dong, L. Wang, Y.-M. Huang, L. Comisso, and A. Bhattacharjee (2018), *Role of the Plasmoid Instability in Magnetohydrodynamic Turbulence*, Physical Review Letters **121**, 165101. DOI.

[42] C. Dong, L. Wang, Y.-M. Huang, L. Comisso, T. A. Sandstrom, and A. Bhattacharjee (2022), *Reconnection-driven energy cascade in magnetohydrodynamic turbulence*, Science Advances **8**, eabn7627. DOI.

[43] E. G. Zweibel and M. Yamada (2009), *Magnetic Reconnection in Astrophysical and Laboratory Plasmas*, Annual Review of Astronomy and Astrophysics **47**, 291–332. DOI.

[44] E. G. Zweibel and M. Yamada (2016), *Perspectives on magnetic reconnection*, Proceedings of the Royal Society A **472**, 20160479. DOI.

[45] M. Yamada, R. Kulsrud, and H. Ji (2010), *Magnetic reconnection*, Reviews of Modern Physics **82**, 603–664. DOI.

[46] G. Vekstein (2016), *Storing free magnetic energy in the solar corona*, Journal of Plasma Physics **82**, 925820401. 10.1017/S0022377816000726. Section 4 gives the coronal resistive-diffusion estimate.

[47] I. T. Chapman (2011), *Controlling sawtooth oscillations in tokamak plasmas*, Plasma Physics and Controlled Fusion **53**, 013001. 10.1088/0741-3335/53/1/013001. Review of the sawtooth cycle, trigger physics, and implications for fusion operation; open-access version.

[48] Y.-H. Liu, M. Hesse, K. Genestreti, et al. (2025), *Ohm's Law, the Reconnection Rate, and Energy Conversion in Collisionless Magnetic Reconnection*, Space Science Reviews **221**, 16. 10.1007/s11214-025-01142-0. Open-access tutorial review.

[49] N. F. Loureiro and D. A. Uzdensky (2016), *Magnetic reconnection: from the Sweet–Parker model to stochastic plasmoid chains*, Plasma Physics and Controlled Fusion **58**, 014021. 10.1088/0741-3335/58/1/014021. Open manuscript.

[50] L. Sironi, D. A. Uzdensky, and D. Giannios (2025), *Relativistic Magnetic Reconnection in Astrophysical Plasmas: A Powerful Mechanism of Nonthermal Emission*, Annual Review of Astronomy and Astrophysics **63**, 127–178. 10.1146/annurev-astro-020325-115713. Open manuscript.

[51] D. A. Uzdensky (2016), *Radiative Magnetic Reconnection in Astrophysics*, in *Magnetic Reconnection: Concepts and Applications*, edited by W. Gonzalez and E. Parker, Astrophysics and Space Science Library **427**, pp. 473–519, Springer. 10.1007/978-3-319-26432-5_12. Open manuscript.

[52] A. Lazarian, G. L. Eyink, A. Jafari, G. Kowal, H. Li, S. Xu, and E. T. Vishniac (2020), *3D turbulent reconnection: Theory, tests, and astrophysical implications*, Physics of Plasmas **27**, 012305. 10.1063/1.5110603. Open manuscript.

[53] A. A. Schekochihin (2022), *MHD turbulence: a biased review*, Journal of Plasma Physics **88**, 155880501. 10.1017/S0022377822000721. Open manuscript.

Recommended Reading

Where to start. Item 1 is the main recommended tutorial. Item 2 gives a short overview, and item 3 follows the Sweet–Parker-to-plasmoid sequence in these notes. Use item 4 as a detailed reference; choose items 5–8 according to your interests. Each entry identifies a reading focus and its connection to the lectures.

1. First priority: a tutorial on collisionless reconnection

Y.-H. Liu, M. Hesse, K. Genestreti, et al. (2025), *Ohm's Law, the Reconnection Rate, and Energy Conversion in Collisionless Magnetic Reconnection*, *Space Science Reviews* **221**, 16 [48]. Read the open-access article.

Reading focus: begin with the introduction, then Sections 2, 3.1, and 4: breaking flux freezing, the rate of symmetric reconnection, and energy conversion. Read Section 3.2 for asymmetric dayside reconnection. This is the closest tutorial companion to our discussion of generalized Ohm's law, ion/electron diffusion regions, fast reconnection, and energy budgets (Sections 1 and 9 of these notes). Its main topics can be read separately.

For a shorter companion on the rate question: P. A. Cassak, Y.-H. Liu, and M. A. Shay (2017), *A review of the 0.1 reconnection rate problem*, *Journal of Plasma Physics* **83**, 715830501 [31]. Article.

2. Broad physical context: why reconnection matters

E. G. Zweibel and M. Yamada (2016), *Perspectives on magnetic reconnection*, *Proceedings of the Royal Society A* **472**, 20160479 [44]. Open article.

Reading focus: the connection between magnetic topology, energy release, and the coupling of microscopic layers to large-scale systems. Use this perspective to connect the solar, magnetospheric, and laboratory examples in Section 1 to the central questions of the course. For a longer companion, see the same authors' *Magnetic Reconnection in Astrophysical and Laboratory Plasmas* (2009), *Annual Review of Astronomy and Astrophysics* **47**, 291–332 [43]. Open article.

3. From Sweet–Parker layers to plasmoid-dominated reconnection

N. F. Loureiro and D. A. Uzdensky (2016), *Magnetic reconnection: from the Sweet–Parker model to stochastic plasmoid chains*, *Plasma Physics and Controlled Fusion* **58**, 014021 [49]. Open manuscript.

Reading focus: Sections 1–2, especially why a long, thin layer becomes unstable and how nonlinear plasmoid chains change the reconnection picture. This directly supports Sections 5–7 of these notes. On a first pass, focus on the physical arguments and scaling results; the detailed tearing calculation can be deferred.

4. A comprehensive reference for theory, experiments, and observations

M. Yamada, R. Kulsrud, and H. Ji (2010), *Magnetic reconnection*, *Reviews of Modern Physics* **82**, 603–664 [45]. Open article.

Reading focus: Section II for observed examples, Section III for classical theory, and Section VI for two-fluid physics and diffusion-region structure. Consult the relevant part when revisiting a lecture, rather than reading this long review straight through. Pair its foundational treatment with item 1 for more recent collisionless results.

Recommended Reading: topical extensions

5. Relativistic reconnection and high-energy emission

L. Sironi, D. A. Uzdensky, and D. Giannios (2025), *Relativistic Magnetic Reconnection in Astrophysical Plasmas: A Powerful Mechanism of Nonthermal Emission*, *Annual Review of Astronomy and Astrophysics* **63**, 127–178 [50]. Published review; open manuscript.

Reading focus: start with the relativistic regime and kinetic-simulation picture, then follow particle acceleration, plasma heating, and radiation into the astrophysical applications. This is the main recommended high-energy review for Section 10 of these notes. Ask how the upstream magnetic energy is divided among bulk motion, thermal particles, nonthermal particles, and emitted radiation.

6. When radiation changes the reconnection dynamics

D. A. Uzdensky (2016), *Radiative Magnetic Reconnection in Astrophysics*, in *Magnetic Reconnection: Concepts and Applications*, edited by W. Gonzalez and E. Parker, Springer, pp. 473–519 [51]. Book chapter; open manuscript.

Reading focus: radiative cooling, radiation-reaction limits on acceleration, and their feedback on reconnection. Compare cooling and dynamical times, and identify which terms alter the energy budget. This more specialized chapter complements item 5 and the radiative examples in Section 10; select an astrophysical application after reading the basic physical discussion.

7. How turbulence changes reconnection

A. Lazarian, G. L. Eyink, A. Jafari, et al. (2020), *3D turbulent reconnection: Theory, tests, and astrophysical implications*, *Physics of Plasmas* **27**, 012305 [52]. Published review; open manuscript.

Reading focus: magnetic-field-line wandering, stochastic flux transport, and the role of a broadened outflow region. This develops the turbulent-background picture in Section 11 of these notes. Read it alongside item 8: the two reviews emphasize different mechanisms and contain differing assessments of when each controls the dynamics. Compare their assumptions about geometry, scales, and times.

8. How reconnection changes a turbulent cascade

A. A. Schekochihin (2022), *MHD turbulence: a biased review*, *Journal of Plasma Physics* **88**, 155880501 [53]. Published review; open manuscript.

Reading focus: Section 7, on the interaction of MHD turbulence with reconnection. Follow the comparison between a tearing growth time and an eddy lifetime, and how disruption can alter the cascade. This is the most direct bridge from our turbulence lectures to the final part of Section 11. Section 12 of the review is an optional extension on decaying turbulence; detailed asymptotic derivations can be left for a second reading.